vol. 45, n.° 1, enero-abril de 2023
ISSN impreso: 0120-0283 • ISSN en línea: 2145-8553

Mineralogical, petrographic, and geochemical analyzes which confirm the hydrothermal origin of the sediments that overlie the peridotites of Cerro Matoso, Colombia

Andrés Castrillón[1*]; Franck Lartaud[2]; Antonio Delgado-Huertas[3]; Fernando Núñez-Useche[4]

[1]Departamento de Geociencias, Universidad Nacional de Colombia, Bogotá, Colombia. (*) acastrillonp@unal.edu.co
[2]Laboratoire d'Ecogéochimie des Environnements Benthiques (LECOB), Sorbonne Université, France. franck.lartaud@obs-banyuls.fr
[3]Instituto Andaluz de Ciencias de la Tierra, Universidad de Granada, Granada, Spain. antonio. delgado@csic.es
[4]Instituto de Geología, Universidad Nacional Autónoma de México, Ciudad de México, México. fernandonu@geologia.unam.mx

Abstract

The Cerro Matoso deposit, one of the largest open-pit ferronickel mines in the world is formed by a sedimentary succession on top of an abducted ultramafic body that makes part of the Cauca ophiolite complex. The set of rocks was accreted in northwestern Colombia during the Cretaceous and exposed to weathering processes during the last Andean Orogeny. Sediment samples were collected and studied using petrographic microscopy, SEM, EPMA, ICP-MS, XRF, and oxygen as well as carbon isotopes analyses. Oxygen isotope results reflect pore-water temperatures reaching up to 130°C during mineral precipitation, which are consistent with serpentinization-derived fluids of mantle rocks that may be related to deep-sea hydrothermal activity. Negative $\delta^{13}C$ values (–27.1 to –1‰ V-PDB) in bulk samples of the tabular succession correlate with the $\delta^{13}C$ range of methane from modern serpentinite-derived fluids. The REE/Fe data (ratio <0.4) suggest that sediments differenced in black mudstone and fossiliferous green claystone correspond to metalliferous and hydrothermal sediments respectively, formed in the ancient mid-ocean Pacific ridge, far west of its present position. Positive Eu and negative Ce anomalies registered in the black mudstone succession correlate with a hydrothermal plume scenario.

Keywords: Oxygen and carbon isotopes; Methane; REE; Hydrothermal vent systems; Nickel laterites.

Análisis mineralógicos, petrográficos y geoquímicos confirman el origen hidrotermal de sedimentos metalíferos sobreyaciendo las peridotitas de Cerro Matoso, Colombia

Resumen

El yacimiento Cerro Matoso, una de las minas de ferroníquel a cielo abierto más grandes del mundo, está formado por una sucesión sedimentaria que reposa sobre un cuerpo ultramáfico adosado al continente, que forma parte del Complejo Ofiolítico del Cauca. El conjunto de rocas fue adosado en el noroeste de Colombia durante el Cretácico, y fue expuesto a procesos de meteorización durante la última

How to cite: Castrillón, A.; Lartaud, F.; Delgado-Huertas, A.; Núñez-Useche, F. (2023). Mineralogical, petrographic, and geochemical analyzes which confirm the hydrothermal origin of the sediments that overlie the peridotites of Cerro Matoso, Colombia. *Boletín de Geología, 45*(1), 53-86. https://doi.org/10.18273/revbol.v45n1-2023003

orogenia andina. Las muestras de sedimentos fueron recolectadas y estudiadas mediante microscopía petrográfica, SEM, EPMA, ICP-MS, FRX y análisis de isótopos de oxígeno y carbono. Los resultados de los isótopos de oxígeno reflejan temperaturas del agua intersticial que alcanzan los 130°C durante la precipitación mineral, lo que es coherente con fluidos derivados de la serpentinización de las rocas ultramáficas que pueden estar relacionados con actividad hidrotermal en el fondo del mar. Los valores negativos de $\delta^{13}C$ (−27,1 a −1‰ V-PDB) en muestras (roca total) de la sucesión sedimentaria, se correlacionan con el rango de $\delta^{13}C$ del metano de fluidos modernos derivados de serpentinita. Los datos REE/Fe (relación <0.4) sugieren que los sedimentos denominados lodolitas negras y arcillolitas verdes fosilíferas corresponden a sedimentos metalíferos e hidrotermales respectivamente, formados en la antigua dorsal meso-oceánica del océano Pacífico, muy al oeste de su posición actual. Las anomalías positivas de Eu y negativas de Ce registradas en la sucesión de lodolitas negras se correlacionan con un escenario de plumas hidrotermales.

Palabras clave: Isótopos de oxígeno y carbono; Metano; REE; Sistemas de ventilas hidrotermales; Lateritas de níquel.

Introduction

Ancient sediments are a window into the past and, through the analysis of fossils, isotope fingerprints, geochemical composition, and mineralogy, it is possible to understand the coevolution of the planet with life. Peridotites are mantle rocks commonly exposed in oceanic fracture zones and along low-angle faults related to tectonic extension and crustal thinning at slow-spreading mid-ocean ridges (*e.g.*, Escartín *et al*., 2003; Mével, 2003; Alt *et al*., 2007). The oceanic peridotites are subject to an intense activity driven by heat supply provided by the intrusion of mafic magmas or by cooling of the ultramafic lithosphere which produces serpentinization and fluid circulation (Alt *et al.,* 2007). These create a hydrothermal environment that can support vent communities (*e.g*., Kelley *et al*., 2001). Oxygen isotope data from the Hess Deep in the Pacific Ocean, indicate that serpentinization of the upper mantle occurs at temperatures of 275–375ºC when seawater penetrated downward during rifting related to the propagation of the Galapagos spreading center (Agrinier *et al*., 1995; Früh-Green *et al*., 1996; Alt *et al.,* 2007). However, serpentinization reactions can also take place at relatively low temperatures (0–150ºC) in fluid vent sites where microbial activity has been detected (*e.g.,* Agrinier *et al.,* 1995; Alt and Shanks, 1998; Kelley *et al.,* 2001, 2005; Alt *et al.,* 2007). Different fine-grained type sediments can be associated with the activity surrounding hydrothermal vent systems hosted by ultramafic rocks exposed in the oceanic fractures and mid-ocean ridges (*e.g*., Früh-Green *et al*., 2004; Ludwig *et al*., 2006). Metalliferous sediments have been associated with hydrothermal systems occurring on various spatial and time scales principally in ocean ridges. The metal enrichment has been attributed to high-temperature hydrothermal sources (Mills and Elderfield, 1995a), but also to a low-temperature hydrothermal activity supported by oxygen isotope studies of nontronite within the sediment (*e.g.,* McMurtry and Burnett, 1975; McMurtry and Yeh, 1981) or with the transport of particles by bottom currents in deep fracture zones of the East Pacific Ridge (EPR) (Heath and Dymond, 1981). Mills and Elderfield (1995a) documented in the Pacific Ocean the formation of basal metalliferous sediment that overlies igneous crust. These deposits consist of poorly crystalline to X-ray amorphous Fe-Mn-oxyhydroxides, clay minerals, and amorphous silicate phase (Dekov *et al*., 2010). The oxyhydroxides furthermore are efficient scavengers for rare earth elements (REE) and Yttrium along with others trace elements such as Ni, Co, and Cu (Ruhlin and Owen, 1986; Mitra *et al*., 1994; Hein *et al*., 1997; Kuhn *et al*., 1998). Metalliferous sediments are characterized by a very high Fe and Mn content (on an abiogenic basis), very low Al/(Al + Fe + Mn), high content (on an abiogenic basis) of As, Ba, Be, Bi, Cd, Co, Cu, Mo, Ni, Pb, Sb, Th, U, V, W, Y, Zn, and Zr and depleted in Al (and Ti) relative to pelagic background sediments (Dekov *et al.,* 2010). Their REE distribution patterns are like that of deep seawater and show weak signs of hydrothermal imprint (weak positive Eu anomaly). Metalliferous (hydrothermal) sediments distributed on ridges are associated with the deposition of metal-rich phases from near volcanic emanations (Boström and Peterson, 1969; Slack *et al*., 2009), and have been linked to the combination of hydrothermal plume fallout of Fe and Mn oxyhydroxide, mass-wasting of sulfide mound debris, and sedimentation of detrital and biogenic particles (Metz *et al*., 1988; German *et al*., 1993; Mills *et al*., 1993; Mills and Elderfield, 1995a; German and Von Damm, 2003).

REE distribution pattern in metalliferous sediments provides valuable information about the elemental source and dissolved oxygen levels (Byrne and Sholkovitz, 1996; Nozaki, 2001; Nozaki and Alibo,

2003). REE patterns vary from fluid to seawater by both scavenging of particles in the water column (Byrne and Sholkovitz, 1996; Nozaki, 2001) and fractionation from the hydrothermal fluids during precipitation (Mitra *et al*., 1994; Mills and Elderfield, 1995b). The REE behavior in high-temperature seafloor hydrothermal fluids is well characterized (Michard and Albarede, 1986; Klinkhammer *et al*., 1994). Highly enriched REE concentrations in high-temperature hydrothermal vent fluids up to 10×10^4 times ambient seawater concentrations have been measured in several sites: Trans-Atlantic Geotraverse (TAG) chimney oxides from Mid-Atlantic Ridge (MAR) (Mills and Elderfield, 1995b); Juan de Fuca Ridge (Hinkley and Tatsumoto, 1987), Snake Pit area also called MARK site along MAR at 23°N (Campbell *et al*., 1988) and East Pacific Rise at 13°N and 21°N (Michard *et al*., 1983; Michard and Albarede, 1986). Black smoker fluids exhibit a distinct REE pattern with light REE (LREE) enrichment, a large Eu anomaly, and negative or no Ce anomaly (Klinkhammer *et al.,* 1994; Mitra *et al.,* 1994). This pattern is distinct from seawater which has no Eu anomaly, a large Ce anomaly, and heavy REE (HREE) enrichment (Mills and Elderfield, 1995b). According to Klinkhammer *et al.* (1994), hydrothermal fluids may represent a significant secondary source of REEs (especially Eu) in the oceans. REE-Y patterns are commonly used to trace the origin of metalliferous deposits (Sui and Lasby, 1998). Recently, using REE elements relations Hodel *et al*. (2018) demonstrate that the Aït Ahmane ultramafic unit of the ca. 760 Ma Bou Azzer ophiolite (Morocco) hosts a fossil black smoker-type hydrothermal system.

In northwest Colombia, at the northern end of the western Andean Cordillera, a set of rocks formed by claystone and mudstone rests on top of the Cerro Matoso peridotites (Castrillón, 2019). The set of rocks was accreted during the Cretaceous and later exposed to weathering conditions. The peridotites developed a nickel laterite profile from which is mined, molten, and processed to produce, in one of the largest lateritic nickel mines worldwide, an alloy of iron and nickel of high purity and low carbon content, for exportation to the international markets, mainly Asia. Recently, Castrillón *et al*. (2022), using XRD, BSE-EDX, and SEM analyses, described petrographic and mineralogical characteristics of the claystone/mudstone overlying the Cerro Matoso peridotites in the Pit-1, north of the mine. The XRD analysis permitted the identification of siderite as the only carbonate in the samples and petrographic and SEM studies allowed classifying the siderite as a diagenetically altered mineral that are infilling cracks, pores, and pipes acting as a cement. These sediments were identified as deep marine claystone forming mound structures and black mudstone forming tabular beds.

Here, new petrographic and mineralogical data combined with oxygen and carbon isotopes, EPMA, and ICP-MS analyses, including trace elements and REE+Y distribution from the claystone and mudstone on top of the Cerro Matoso peridotites, are presented as novel evidence of the formation of deep-marine sediments hosted by peridotites with serpentinization-related and released fluids from the mantle section of the ancient mid-ocean Pacific ridge. This improves our understanding of the mechanisms involved in the formation of the Cerro Matoso metalliferous sediments.

Regional setting

The Cerro Matoso deposit is in northwest Colombia, about 100 km southeast of Montería in the province of Córdoba, in the northern end of the Western Andean Cordillera. The peridotite body occurs in one of a series of isolated outcrops assigned to the Cauca ophiolite complex of the Early Cretaceous age (Mejia and Durango, 1981). This complex is a relict of oceanic crust originated in the Pacific Ocean, far west of its present position (Pindell and Barrett, 1991; Pindell and Kennan, 2009). The ophiolitic complex of which Cerro Matoso is part was tectonically accreted during the Pre-Andean orogeny along the Romeral Fault System, considered as a major boundary between oceanic crust to the west and continental crust to the east (Barrero, 1974; Meissnar *et al*., 1976). Migration of the American continent to the west and of the oceanic plate to the east caused the accretion of oceanic segments to the western margin of the continent (Lewis *et al*., 2006). Probably the emplacement of Cerro Matoso and Planeta Rica peridotites took place during the pre-Andean orogeny (Middle Eocene) and from that moment, the laterization process began (Dueñas and Duque-Caro, 1981; López-Rendón, 1986; Hoyos and Velázquez, 1996). The ultimate exhumation and ultramafic rocks exposition to the supergene weathering conditions was during the Andean orogeny (Figure 1). The ultramafic rocks are surrounded by basalts (Ksvb) (outcropping 30 km to the south), and the sedimentary succession from early to mid-Miocene that includes a transgressive succession consisting of fluvial and shore sandstones (Ciénaga de Oro Formation-Pgoco), followed by marine shales (Porquera Formation-Ngmpc) interpreted to unconformably overlie the oceanic rocks. Finally, marine sediments (Cerrito Formation-Ngmc and Sincelejo Formations-NgQsi) unconformably overlie the Porquera Formation.

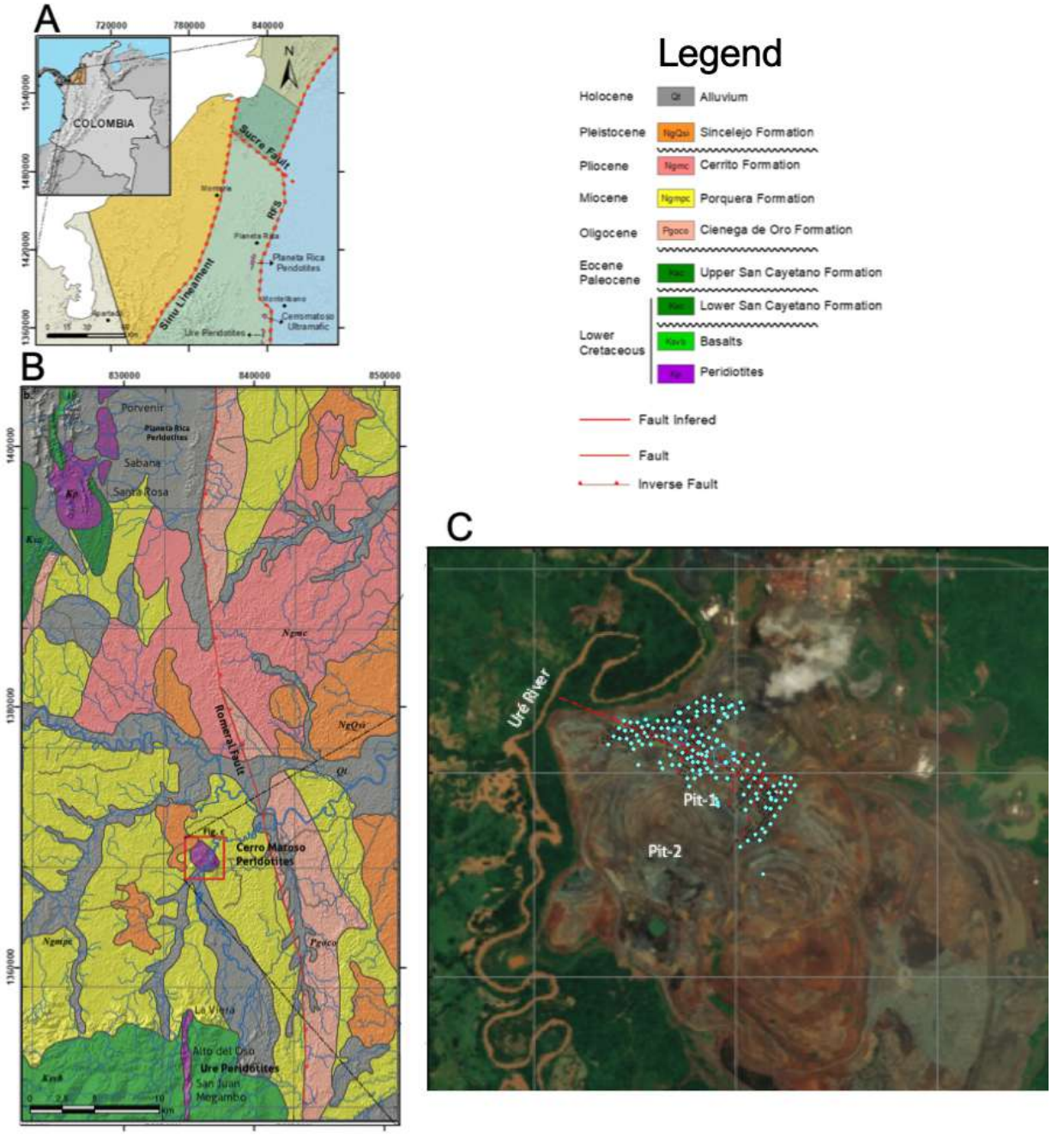

Figure 1. A. Cerro Matoso regional location. **B.** Cerro Matoso peridotites are unconformably covered by the latest Oligocene to Pleistocene strata, including the Ciénaga de Oro (Pgoco), Porquera (Ngmpc), Cerrito (Ngmc), and Sincelejo (NgQsi) Formations. Modified from the SGC Geological maps 72 and 82 (Pueblo Nuevo and Montelibano) and from Tobón *et al*. (2020). **C.** Cian dots show the sedimentary distribution of the black mudstone succession at Pit-1 with a thickness varying between 10 to 20 m.

Local geology

According to López-Rendón (1986), lateritization probably started in the late Eocene-early Oligocene, and chemical weathering and erosion continued through Oligocene. The laterite profile and Ni enrichment in Cerro Matoso suggest different episodes of weathering during the Cenozoic (Gleeson *et al*., 2004). According to López-Rendón (1986), the laterites of Cerro Matoso consist of 5 main horizons from base to top: unaltered peridotite, saprolitized peridotite, saprolite, limonite, and iron hat (gossan) or ¨duricrust¨. Gleeson *et al.* (2004) describe 2 different alteration profiles at Cerro Matoso, one developed on Pit-1 toward the N sector of the mine and the other on Pit-2 toward the S sector and identified in both pimelite and sepiolite as the major nickel-bearing silicate phases, followed by smectites (saponite) and chlorites (nimite). Seven horizons have been described in the laterite profile of Cerro Matoso at the Pit-1 (Gleeson *et al.,* 2004; Tobón *et al*., 2020), although four of these units named: ¨black saprolite¨,¨ black canga¨,¨red laterite¨, and ¨canga mona¨(*e.g.,* López-Rendón, 1986; Ortiz, 2004; Sumicol, 2002; Gleeson *et al.,* 2004; Tobón *et al.,* 2020) were redefined as deep marine claystone/mudstone by Castrillón (2019). At south or Pit-2, the peridotite alters to saprolitized peridotite, high and low-magnesium green saprolites, brown saprolite, and high and low iron laterites, without ferricrete or duricrust. The nickel content at Pit-1 overpassed 9% while at Pit-2 did not surpass 4%.

Methodology

A representative set of 34 samples were collected at the 49 Bench level of Pit-1, where crops out the marine sediments (Figure 1B). The sediments are differenced by 1) a mound structure succession composed of fossiliferous claystone and mudstone at the base (Table 1, Figure 2A-2D), and 2) a tabular bed succession formed by orange iron laminated claystone and fossiliferous red claystone (Figure 2E) that lie over black mudstone that contains intraclast of serpentine and red claystone (Figure 2F-2I). The latter are overlaying listvenites, which also present two varieties (Figure 2J-2K). The listvenites are capping green saprolites (Figure 2L). Downwards the laterite profile is completed of altered peridotites (Figure 2M), peridotites with magnesite veins (Figure 2N), and peridotites (Figure 2O).

A total of 42 subsamples of the greenish and blackish sediments for analysis were extracted from the internal regions of the original rock sample to avoid contamination. All subsamples were cleaned and subdivided into polished, resin-free rock chips and freshly broken fragments. Petrography was done using the binocular and petrographic microscope Carl ZEISS Primo Star HD/Full Köhler cam, 100x, SF2, from the Instituto de Geología of the Universidad Nacional Autónoma de México. Specimens were examined in hand samples and a microscopic study on transmitted and reflected light was made. Isotopic analysis was done on bulk samples, and samples of siderite concretions. This analysis was accomplished by reacting a subsample (10–48 mg dry weight) with 100% phosphoric acid in a Pyrex vessel at 50°C. The reaction was terminated after 10 days, at which time CO_2 was no longer produced, and the reaction was considered completed (Al-Aasm *et al*., 1990).

Table 1. Summary of samples collected at Cerro Matoso Bench 49, Pit-1.

Rock name	Sample cm Id*	Total
Orange iron laminated claystone	46	1
Red claystone	13	1
Green Fossiliferous claystone	10, 21, 22, 23, 24, 25, 32, 33	8
Fissured brecciated mudstone	11	1
Black mudstone	19, 20, 26	3
Intraclast	1, 2, 5, 9, 35	5
Listvenites	3, 4, 6, 7, 18, 27	6
Green saprolite	12, 34	2
Saprolitized peridotite	15, 17, 28, 30	4
Peridotite	16, 29	2
Serpentinized peridotite	14	1

Note: *Related with Table 4.

Figure 2. Hand samples collected from the Cerro Matoso deposit at Pit-1. **A.** Brown oxidized claystone. **B-C.** Green fossiliferous claystone. **D.** Fissured brecciated mudstone. **E.** Fossiliferous red claystone. **F.** Intraclast of serpentinite. **G.** Intraclast of red claystone. **H.** Black mudstone facies II. **I.** Black mudstone facies I. **J.** Listvenite variety A is characterized by brecciated textures with high silica/siderite vein content. **K.** Listvenite variety B is characterized by a purple color. **L.** Low-Mg green saprolite. **M.** Saprolitized peridotite. **N.** Magnesite and silica veins in peridotite. **O.** Fresh peridotite.

The evolved CO_2 was used for the calculation of siderite abundance in the subsample and the analysis of oxygen and carbon isotope compositions. Isotope measurements were carried out at the Stable Isotope Laboratory of the Instituto Andaluz de Ciencias de la Tierra (CSIC, Granada, Spain). Isotopic ratios were measured by a Finnigan MAT 251 mass spectrometer. The reproducibility of the analytical procedure was lower than ±0.2‰ for carbonate Fe-Mg. All the samples were compared to a carbon dioxide sample obtained from siderite and calcite standards prepared at the same time. A fractionation factor (αsiderite-CO_2) of 1.01006 (Rosenbaum and Sheppard, 1986) was used to back-calculate the isotopic compositions of siderite due that CO_2 has a different oxygen isotope composition than siderite, from which the gas was evolved (*e.g.,* Zhang *et al*., 2001). Oxygen and carbon isotopes of siderite were reported relative to the standard – Vienna Pee Dee

Belemnite (V-PDB). Oxygen data were also converted into SMOW using the Coplen *et al*. (1983) equation: $\delta^{18}O‰$ (SMOW) = 1.03090 × $\delta^{18}O‰$ (V-PDB) + 30.91 to investigate the relationship with temperature. The isotopic modeling for carbon considered a marine environment with an isotope pool of H_2S, CH_4, OH^-, HCO_3^- and Fe, where $CaCO_3$ and CH_4 are products of the isotopic exchange during an electron loss and gain process. The fractionation factor resulting from anaerobic or aerobic oxidation of methane was 1.039 (Whiticar and Faber, 1986; Templeton *et al*., 2005) and was considered the maximum value of the isotopic fractionation Δ = 39‰, for product 1 or $CaCO_3$. The residual substrate or product 2 (CH_4), takes a Δ_2 = 12.3‰ value which represents the highest isotopic depletion in the aqueous medium. An equilibrium constant of kinetic isotope effect KIE = –32 was considered. The fractionation model for $\delta^{18}O$ considered O_2 and $CaCO_3$ as products 1 and 2 that are generated in the process of electron loss and gain in an open system. The isotopic fractionation Δ = –31‰ for O_2 was suggested by Fu *et al*. (2015) for hydrothermal systems and for $CaCO_3$ the Δ_2 = 10‰ was suggested by Li *et al*. (2006). The equations used for the isotopic modeling were:

1) Δ pool = Δ 2 + f + Δ 1 – Δ 2 × f
2) $f^{13}C = 1 – (\delta^{13}C‰(V\text{-}PDB)/KIE)$, KIE = –32
3) $f^{18}O = 1 – (\delta^{18}O‰(V\text{-}PDB)/KIE)$, KIE = 10
4) ln = LN (f)
5) $\alpha = (1000 + KIE)/(1000 + \delta^{18}O‰(PDB))$
6) $10^6 T^2 = 10^3 LN (\alpha) – 1.69/2.56$
7) $\delta^{18}O‰(SMOW) = 1.03090 \times \delta^{18}O‰(PDB) + 30.91$
8) $\delta^{18}O‰(V\text{-}PDB) = \delta^{18}O‰(SMOW) \times 0.97002 - 29.98$
9) $\delta^{13}C‰(V\text{-}PDB) = \delta^{13}C‰(V\text{-}PDB) + (\delta^{13}C‰(V\text{-}PDB) \times 1.95/100)$
10) Oxygen Isotope fractionation = 10^3 LN (α)

Later, thin sections were critically point-dried and coated with a thin layer of carbon to be analyzed with an electron probe microanalyzer (EPMA) JEOL JXA-8900 XR, at the Laboratorio Universitario de Petrología of the Instituto de Geofísica Ambiental, Universidad Nacional Autónoma de México (UNAM). This equipment allowed us to obtain back-scattered electron (BSE) images, together with X-ray energy dispersive spectroscopy (EDS), qualitative analyses, and wavelength dispersive spectroscopy (WDS) for quantitative analysis of the mineral grains. The conditions used during this analysis were: 20 KeV, a beam diameter of 1 µm, and a counting time of 30 s. The measured conditions were for K, Na, Ba, Ca, Sr, Mn, Mg, and Fe with standards of Guaymas Data. This analysis provides data on the chemical composition of carbonates. The analysis focused on the oxides content of Fe carbonates, magnetite, and clays. The results were normalized for CO_2.

Bulk-rock chemical analysis of 10 samples was performed at Gmas Lab. (Bogotá) by x-ray fluorescence in fused $LiBO_2/Li_2B_4O_7$ disks using a BrukerS4-Explorer X-ray fluorescence spectrometer with an Rh-anode X-ray tube as a radiation source. The semi-quantitative and quantitative analysis was carried out using the QUANT-EXPRESS method (fundamental parameters) before calibration of the equipment with certificated USGS standard samples (AGV1, BCR2, DST2, QLO1, G2, and W2A). Additionally, chemical analysis of 5 bulk-rock samples was performed at Activation Laboratories Ltd (Actlabs) in Canada, with the Ultratrace 5 analytical package (Instrumental Neutron Activation Analysis, INAA + Inductively coupled plasma mass spectrometry, ICP-MS) in a Thermo Finnigan-High Resolution mass spectrometer. The detection limits were 0.01% for major elements and 0.5 ppm for trace elements, with a precision of ±5%. The REE concentrations are normalized relative to the composition of the standard Shales (Piper, 1974). Scanning electronic microscope Hitachi-TM-1000 and the wd/ed microanalyzer JXA-8900R, both from the Instituto de Geofísica Ambiental (UNAM), were used to identify the mineral and chemical components of the selected samples. Standards used for calibration of the equipment included pure metals and synthetic and natural minerals (carbonates and sulfates) from the set of standard SPI # 02753-AB serial No. 02–148.

Results

Field relations

Fossiliferous claystone (mound structures): On top of the peridotites rest a mound structure characterized by a massive and discontinuous unit approximately 14 m high and 50 m long. With a predominantly clay grain size, the claystone unit is characterized by its high porosity, and numerous hollow vug and tubular structures with an orientation that is roughly perpendicular to the base of the mound. The tubes are visible (15 m in diameter) and look like forming colonies. Some tubes are infilled with the same material as the substrate while others are infilled with siderite which also works as cement. This succession is

laterally in contact with black mudstone. From the top, three facies can be differentiated:

In the upper part, a segment of 3 m thickness is formed of brown-colored claystone (bo-C) facies, which is characterized by an apparent layering, rough surfaces, tube structures (9-25 mm in diameter), intraclast and bioclast content (Figure 3A). In thin section, the fossil (*i.e.*, gastropods) content is fully replaced by goethite, the principal mineral identified by XRD (Table 2).

Table 2. Hand sample description and XRD results.

Appearance	Facies name	Hand sample description	Principal minerals XRD (Castrillón, 2019)	Subsample Id
Tabular beds	Black conglomeratic mudstones II	Fine sand to coarse silt size and friable rock with muddy texture. Dark bluish green (5BG 3/2) and very pale green (10G 8/2) colored. Clayish matrix. Magnetic.	Greenalite, nimite, siderite, goethite, magnetite, chromite, Fe oxide	cm-19 54 19
	Black conglomeratic mudstone I	Clayish rock mottled in appearance. Green (10G 8/2) to pale green (5G 7/2) colored, alternating with non-continuous orange, red, and black laminations associated to Fe oxides and manganese.	Greenalite, berthierine, siderite, goethite, manganese oxide, nimite, magnesium sulfate	26
	Serpentine intraclast	Weakly foliated massive hard rock of pale yellowish green in color (10GY 7/2) with phaneritic texture and weakly oriented mafic of very coarse sand size.	Siderite, antigorite, olivine, talc, serpentine, spinel,	9
	Claystone intraclast	Well cemented Claystone. Moderate reddish brown (10R 4/6) and mottled in color.	Greenalite, berthierine, siderite, goethite, nimite, chromite	cm-27 35
Mound structure	Brown oxidized claystone	Well cemented and altered claystone with a low fossiliferous content, very high porosity formed by open conduits, fissures, or burrows, low proportion of intraclast, and bioclast.	Greenalite, goethite	cm-11 23
	Green fossiliferous claystones	Well cemented fossiliferous claystone, with very high porosity formed by open conduits, fissures, or burrows, low proportion of intraclast, and bioclast.	Berthierine, nimite, siderite, goethite	cm-5 32 49
	Fissured brecciated mudstone	Brecciated and fissures (<1mm width) black to dark reddish-brown colored mudstone with fragile and brittle appearance, poorly fossil content. Porosity associated to open conduits, fissures, or burrows.	Siderite, goethite, nontronite	cm-1, 11a

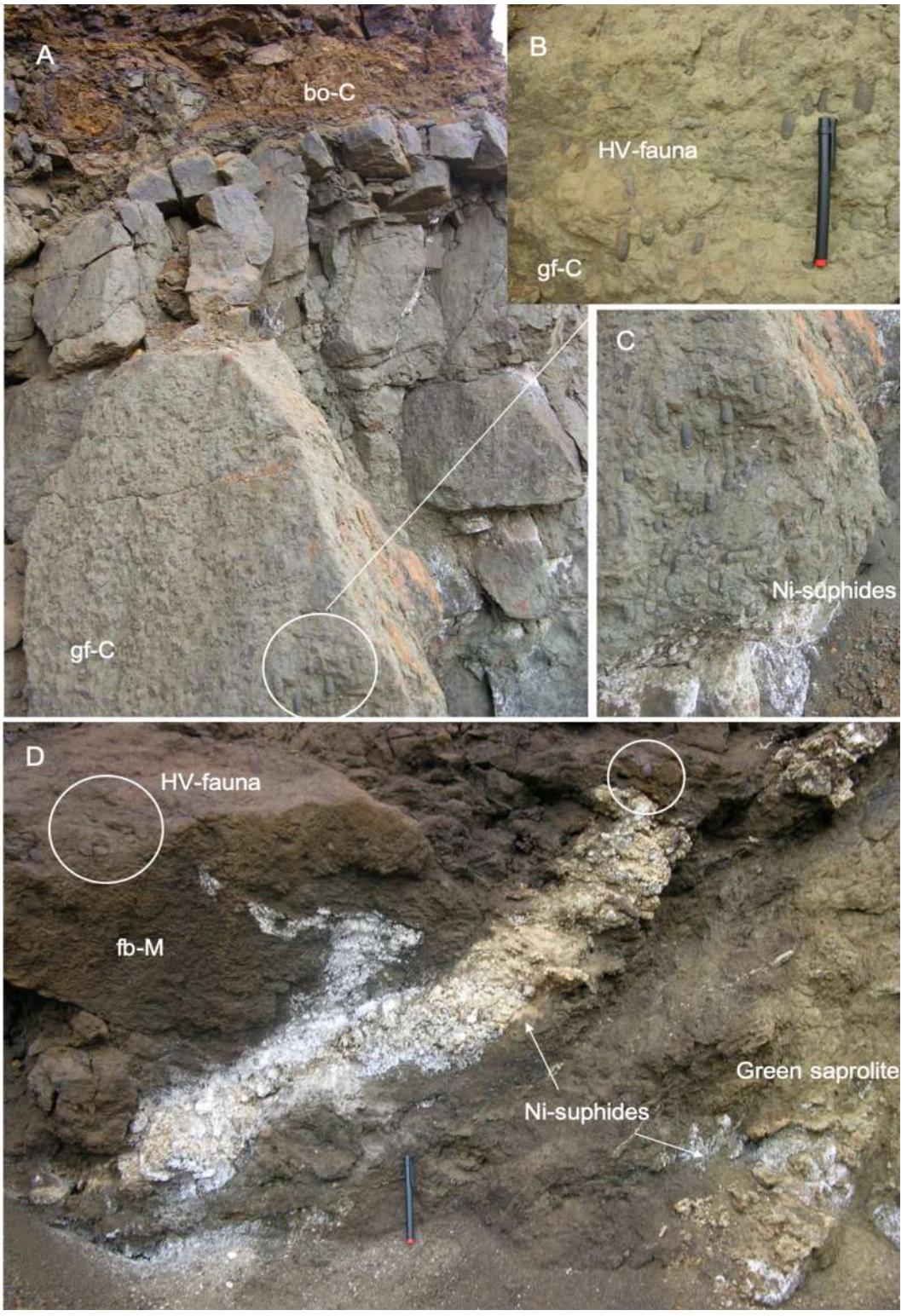

Figure 3. A. Outcrops of brown oxidized claystone (bo-C) overlaying fossiliferous green claystones (gf-C). **B-C.** Detail of tubeworm fossils and vent fauna forming the gf-C facies. **D.** Fissured brecciated mudstone (fb-M) with bioturbation overlaying green saprolites and Ni-sulphides (white) in both units.

Downwards throughout a net contact, a 6 m thickness unit corresponds with green fossiliferous claystone (gf-C) facies, which is characterized by the tube structures and the fossil content that include gastropods, bivalve shells, and tubeworms (15-20 mm in diameter). The fauna is densely packed, some are randomly arranged but many are vertical and appear in a living position (Figure 3B, 2C). Pipes and conduits are common as well as nodules or concretions. In thin section, the green matrix has a low proportion of bioclast and intraclast. Siderite is infilling cracks, pipes, pores, and forms concretions (Figure 4A-4C). Berthierine and siderite were detected in XRD as the major minerals.

Throughout a transitional contact, a 3 m thickness unit is described as a fissured brecciated mudstone (fb-M) underlying the gf-C facies. This unit is characterized by its brittle and fragile appearance, with minor tubular and fossil content. White surfaces over the rocks correspond to Ni-sulphide. In thin section, an intensely fractured or fissured muddy matrix predominates where the siderite is filling the fissures as well as the mold and vug porosity. Gastropods fossils can be recognized. This thin unit rest over green saprolites in which also Ni-sulphides are present.

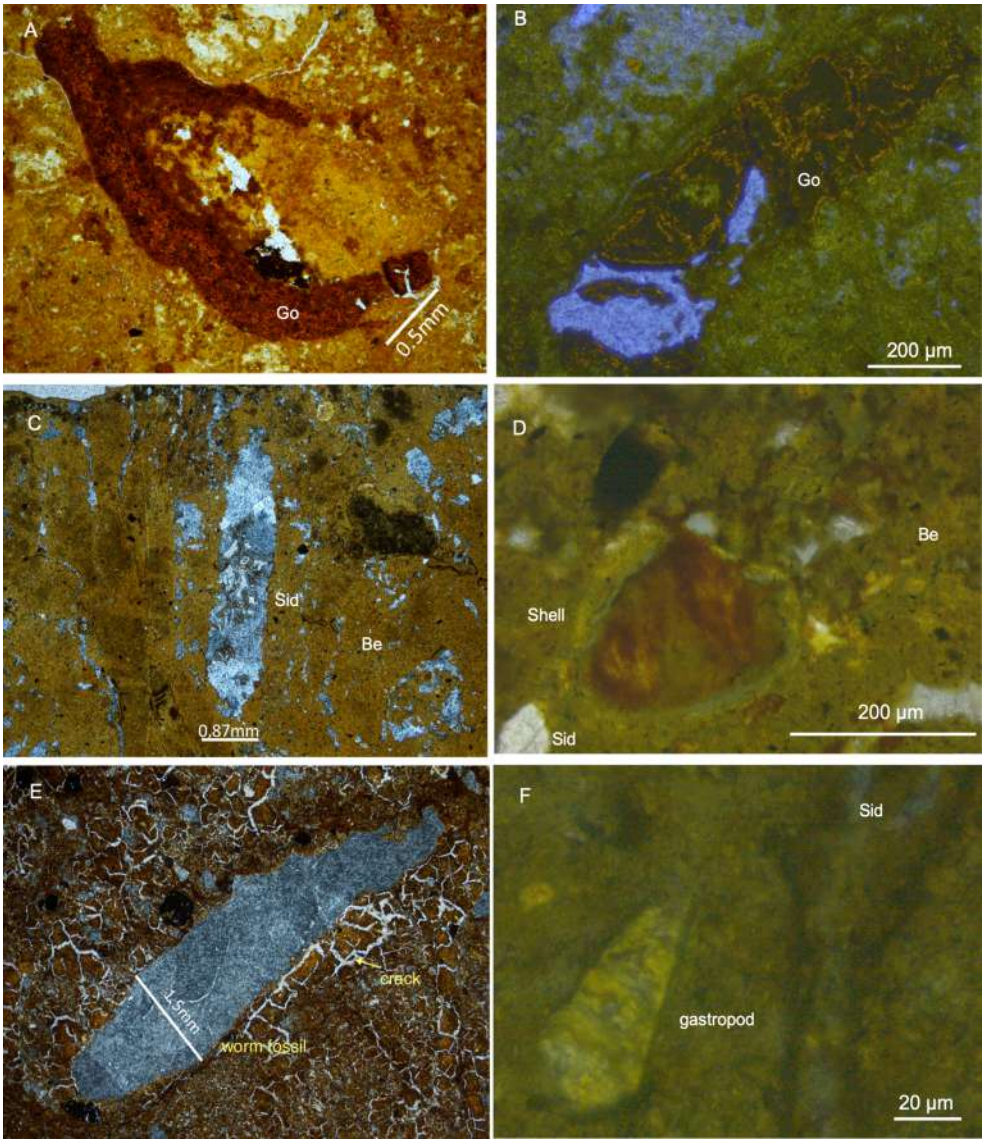

Figure 4. Thin sections. **A.** Brown oxidized claystone forming by goethite and fossil relict. **B.** Detail of fossil relic structure. **C.** Berthierine and siderite forming fossiliferous green claystone facies. Siderite are infilling pores. **D.** Detail of altered shell fossil into the berthierine matrix. **E.** Siderite infilling cracks and pores in the fissured brecciated mudstone. **F.** Gastropod fossil into the fb-M facies.

Iron-rich Mudstones (tabular beds): It is a massive, tabular, and continuous carbonate-Fe-bearing mudstone succession of approximately 40 m of thickness in which three facies can be distinguished. In the upper part, a 4 m thickness unit described as brown orange laminated claystone (oil-C) facies is formed by discontinuous hard beds of Fe-rich claystone in thin layers. Siderite, goethite, and magnetite were detected in XRD as the mayor components (Figure 5A). Throughout a transitional contact, a 20 m of thickness unit described as black mudstone (BM) facies is underlying the oil-C facies. This coarse-grained appearance unit forming tabular beds usually looks extensive and stratified and can be divided into two facies (BM I and BM II).

The upper facies (BM II) is a blackish unit with a brittle and granular mud-sandy appearance, poor cemented and poorly crystallized oxy-oxyhydroxides in a fine matrix (Figure 5B). The framework is composed of bioclasts and intraclasts in a similar percentage, the bioclasts observed are shell fragments and the intraclast are fragments of serpentinites (Figure 6B). In thin section, intraclasts of claystone presents locally wavy laminated structures that have been replaced by goethite and oxides, giving appearances of bioconstructions with siderite and oxides cementing and replacing old bacterial filaments and channels (Figure 6A, sample cm-01). Siderite also is present as part of claystone intraclasts. FeO-rich oxides (magnetite) formed abundantly, usually aligned, straight, and not very continuous. Fragments of olivine, siderite, and Mn-siderite are usual, the latter replacing the fossil structures forming the framework (Figure 6C-6D). Throughout a transitional contact, the BM II facies overlies the BM I facies which is characterized by their pale green / dark green bluish color and a finer grain size or clayish appearance.

Figure 5. A. Orange iron laminated claystone (oil-C) overlaying black mudstone facies. **B.** Black mudstone facies reaching locally a 20 m thickness with claystone and serpentine boulder embedded. **C.** Black mudstone facies overlying listvenites.

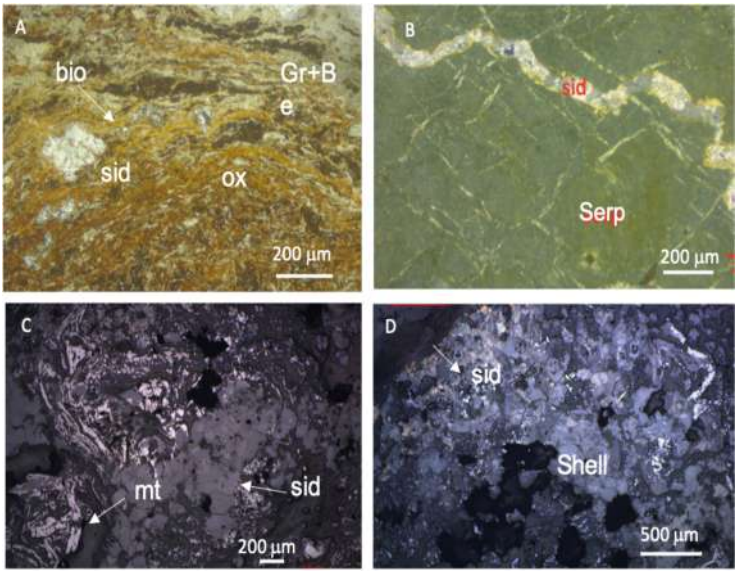

Figure 6. Thin section. **A.** Red clayish intraclast in which bioconstructions formed of finely stratified filaments composed of oxides replacing old biogenic structures in green matrix of greenalite + berthierine with siderite intraclast can be recognized. **B.** Serpentine intraclast composed of serpentinite and siderite infilling cracks. **C.** Black mudstone facies composed of siderite and magnetite. **D.** Bioclast replaced of siderite into the black mudstone facies.

The framework is composed of bioclast and intraclasts in a similar percentage. According to XRD, BM II facies is composed of magnetite (14%) greenalite (10 to 40%), siderite (30-70%), and chromite (<3%), while the BM I facies I is composed of berthierine + greenalite (55%), siderite (38%), and goethite (7%) (Table 2). Laterally, the black mudstone facies are adjacent and/or overlying the green claystone unit but also weathered peridotites (*i.e.*, green saprolites) and listvenites (*i.e.,* metasomatized peridotites) (Figure 5C). Locally, a non-continue succession of red claystone RC composed mainly of goethite with minor fossil content is covering the black mudstone.

EPMA/SEM

A framework with altered fragments of intraclast (*e.g.,* olivine) and bioclast (gastropods) in a clayish matrix (greenalite + berthierine) with abundant Fe-oxides constitute the BM II facies (Figure 7A-7B). Shell fossils in a great alteration state are formed principally by siderite. Fe-rich oxides are in fossil structures. According to EPMA results (wd/ed), the siderite replacing shells is composed of Mn and Mg (Mean ± SD, 1.3%±1.0 and 2.5%±1.2, respectively). The associated oxides are goethite and magnetite (white).

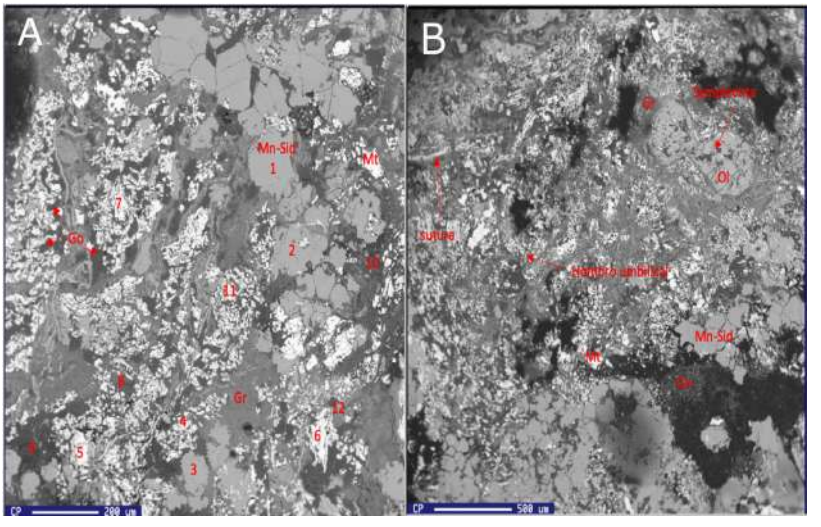

Figure 7. Components of black mudstone and SEM images **A.** Mn-siderite (Mn-sid), magnetite (Mt), goethite (Go), fragments of olivine (Ol), greenalite (Gr). **B.** Gastropod fossil, where the umbilical sector and suture are recognized. Additionally, dissolution appearances are observed in olivine.

The mean ± SD FeO content of siderite is 57.7%±4.4 compared to 83.8%±1.7 of magnetite, while the clays present FeO content of 28.6%±7.4. The olivine presents FeO (16.4%±0.4) and MgO (15.4%±4) (Table 3). SEM observations of BM II facies also revealed barite in the clayish matrix (Figure 8).

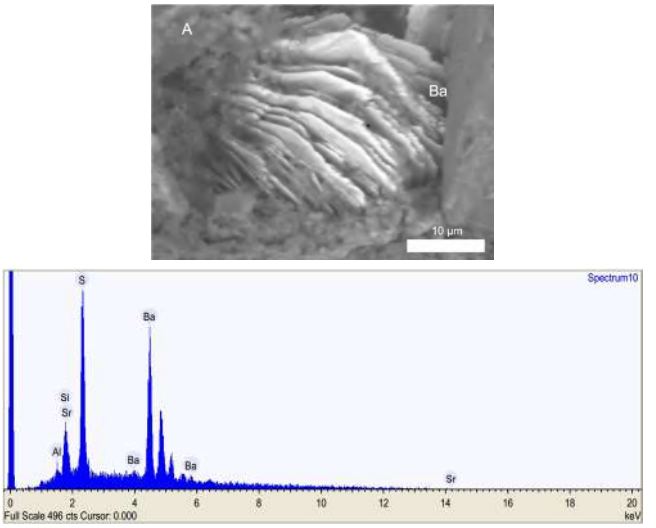

Figure 8. A. Well-formed rhombohedral barite crystals in the fine fraction of the black mudstone facies (SEM image of sample cm-19 rock ship). **B.** Spectrum of principal elements forming the barite crystal.

Table 3. wd/ed Chemical composition of principal minerals in black mudstone II facies.

Mineral	Oxides	wd/ed Chemical composition %			
		Max	Min	Mean	Desv
Siderite	K_2O	0.031	0	0.006	0.009
	Na_2O	0.301	0	0.052	0.091
	MnO	4.078	0.175	1.309	1.063
	SrO	0.021	0	0.002	0.006
	CaO	0.174	0.02	0.069	0.044
	MgO	5.183	0.958	2.505	1.217
	FeO	57.594	37.622	50.362	4.492
	BaO	0.04	0	0.008	0.012
Magnetite	K_2O	0.025	0	0.002	0.006
	Na_2O	0.113	0	0.023	0.03
	MnO	0.549	0.054	0.262	0.147
	SrO	0.018	0	0.003	0.005
	CaO	0.029	0	0.008	0.009
	MgO	0.064	0	0.022	0.025
	FeO	86.159	77.841	83.88	1.712
	BaO	0.065	0	0.019	0.021
Clays	K_2O	0.036	0	0.009	0.009
	Na_2O	0.916	0	0.173	0.238
	MnO	1.651	0.301	0.775	0.33
	SrO	0.053	0	0.014	0.016
	CaO	0.128	0	0.032	0.028
	MgO	3.984	0.891	1.683	0.795
	FeO	39.461	10.789	28.617	7.423
	BaO	0.078	0	0.022	0.029
Relicts olivines	K_2O	0.015	0	0.005	0.007
	Na_2O	0.051	0	0.01	0.023
	MnO	0.156	0.126	0.144	0.011
	SrO	0.857	0.762	0.816	0.039
	CaO	0.021	0	0.011	0.008
	MgO	18.493	10.435	15.446	4.035
	FeO	16.767	15.908	16.444	0.394
	BaO	0.066	0	0.016	0.029

Stable Isotopes

The bulk sediments isotope results from gf-C facies have $\delta^{18}O$ values of −8.7 to −1.8‰ (V-PDB) and $\delta^{13}C$ values of –24.0 to −1.1‰ (V-PDB). Siderite concretions in the green fossiliferous claystone have $\delta^{18}O$ and $\delta^{13}C$ values of −6.4 to −4.1‰ (V-PDB) and −16.0 to −6.0‰ (V-PDB), respectively (Table 4). The dispersion of $\delta^{13}C$ *vs* $\delta^{18}O$ data in the graphic corresponds to different rocks type (Figure 9). The meteoric siderite line (MSL) is drawn as a reference. The bulk sediments isotope analyses of the black mudstone unit indicate $\delta^{18}O$ values of −14.6 to −1.0‰ (V-PDB) and $\delta^{13}C$ values of −21.6 to −8.1‰ (V-PDB), while their intraclast or fragments of green and red claystone have $\delta^{18}O$ and $\delta^{13}C$ values of –10.2 to –4.3‰ (V-PDB) and −27.1 to –16.0‰ (V-PDB), respectively (Table 4).

The temperature estimation involved in the sedimentary minerals in Cerro Matoso was determined using the equation of Carothers *et al*. (1988). The relationship between the fractionation factor and temperature indicates that, depending on the $\delta^{18}O$ values, the green sediment precipitates at temperatures between 25 to 90°C while the black sediments reach 130ºC (Figure 10).

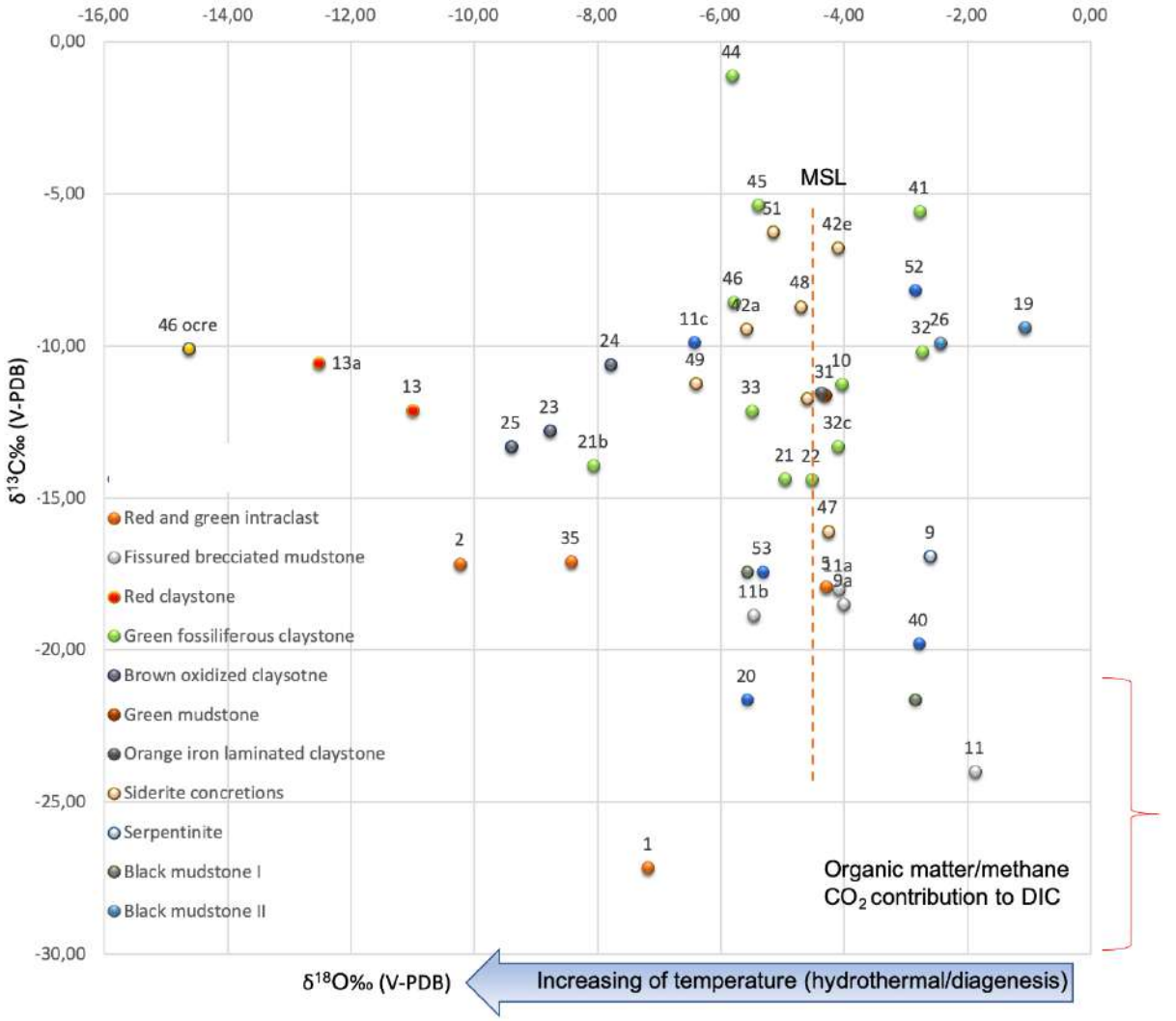

Figure 9. $\delta^{13}C/\delta^{18}O$ (V-PDB) composition of mound succession formed by brown oxidized claystone, green fossiliferous claystone within siderite concretions, and fissured brecciated mudstones facies and the tabular succession formed by orange iron laminated claystones, black mudstones I and II facies and red claystone. For comparison, Meteoric Siderite Line (MSL) have been plotted (vertical dashed line). For the calculus we have used the equation of Carothers *et al*. (1988) considering surficial temperatures 25ºC and low latitude water around –4‰ (V-SMOW). Considering the intervention of marine or diagenetic waters more enriched than 0‰, the calculated temperatures are always above the environmental ones.

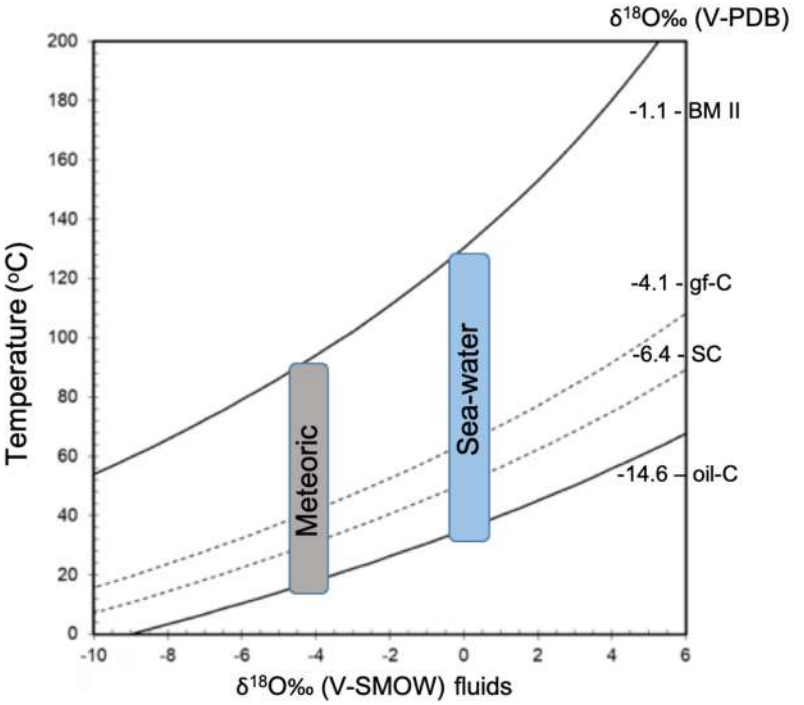

Figure 10. Temperature *vs* $\delta^{18}O$ (water) curves for different $\delta^{18}O$ (siderite) compositions, according to the equations of Carothers *et al.* (1988). Vertical areas of marine water (0‰ *vs* V-SMOW) and low latitude meteoric water around –4‰ (V-SMOW) have been plot for comparison. Curves that relate temperature and isotopic composition of water for different values of siderite are represented.

XRF

The black mudstone facies is composed of silica (SiO_2 = 2.7–12.4 wt.%), high concentrations of iron (Fe_2O_3 = 60.4–79.2 wt.%) and low concentrations of lithophile elements such as Al or Ti (Al_2O_3 = 2.5–5.3 wt.%). In the red claystone interval, the content of Al_2O_3 is 15.3 wt.%. Intraclasts forming black conglomerates mudstone facies have silica (SiO_2 = 10.8–23 wt.%) and iron (Fe_2O_3 = 53.8–72.3 wt.%) that have similar content to fossiliferous green claystone facies. In the latter, the Al_2O_3 is less than 4.8 wt.%. These facies have MgO from 2.4 to 5 wt.%. All facies have similar Ba content (Ba = 125.9–189.6 µg) and variable concentrations of Ni, Cu, Cr, Rb, Sr, and Zn. For comparison, the chemical analyses of mound structure and tabular bed units are in Table 5.

Trace elements and REE

REE was performed for a sample of black mudstone I and II facies (*i.e.,* sample cm-26 and cm-19 respectively), an intraclast into the BM II facies (*i.e.,* reddish claystone, sample cm-35), oil-C facies that is at the top of the succession (sample cm-43) and for green fossiliferous claystone (gf-C) facies (sample cm-32). The results are given in Table 6 and Table 7. A Ce* is defined as follows: Ce*= log (Ce/(2/3La + 1/3Nd)) where Ce, La, and Nd represent the shale-normalized values of each element. Ce* ranges from –2.5 to –0.01. The positive Eu anomaly values above 1 are calculated here using Eu/Eu*= 2Eu/(SmN + GdN), where N represents normalization to Post-Archean Australian Shale (PAAS) (Piper, 1974).

Table 4. $\delta^{13}C$ and $\delta^{18}O$ isotope temperature dependent and modeling calculations for the isotope behavior.

Lithofacies	Sample Id	Facies	ln LN (fraction reacted)	a	10^6T2	Oxygen isotope fractionation $10^3 \times LN\ a$	Fraction reacted $\delta^{18}O$	δ pool ^{18}O	$\delta^{18}O$‰ (SMOW)	$\delta^{18}O$‰ (V-PDB)	$\delta^{13}C$‰ (V-PDB)	δ pool ^{13}C	Fraction reacted $\delta^{13}C$
S	31	GM	0.4	1	8.6	9.3	1.4	-34.4	26.5	-4.3	-11.6	29.3	0.6
Tabular beds	43	oil-C	0.4	1	8.7	9.4	1.4	-34.6	26.4	-4.4	-11.5	29.4	0.6
	46 ocre		0.9	1	19.1	19.7	2.5	-66.3	15.8	-14.6	-10.1	30.6	0.7
	13	RC	0.7	1	15.4	16.1	2.1	-55.1	19.6	-11	-12.1	28.9	0.6
	13a		0.8	1	16.9	17.6	2.3	-59.8	18	-12.5	-10.5	30.2	0.7
	53	BM I and II	0.4	1	9.7	10.3	1.5	-37.5	25.4	-5.3	-17.4	24.5	0.5
	20		0.4	1	9.9	10.6	1.6	-38.3	25.2	-5.6	-21.6	20.9	0.3
	52		0.3	1	7.2	7.8	1.3	-29.8	28	-2.8	-8.2	32.2	0.7
	19		0.1	1	5.4	6.1	1.1	-24.3	29.8	-1.1	-9.4	31.2	0.7
	26		0.2	1	6.8	7.4	1.2	-28.6	28.4	-2.4	-9.9	30.7	0.7
	1	Intraclast	0.5	1	11.5	12.2	1.7	-43.3	23.5	-7.2	-27.1	16.4	0.2
	5		0.4	1	8.6	9.3	1.4	-34.3	26.5	-4.3	-17.9	24	0.4
	2		0.7	1	14.6	15.3	2	-52.7	20.4	-10.2	-17.2	24.7	0.5
	9		0.2	1	6.9	7.6	1.3	-29.1	28.2	-2.6	-16.9	24.9	0.5
	35		0.6	1	12.8	13.4	1.8	-47.1	22.2	-8.4	-17.1	24.7	0.5
Mound Structure	23	bo-C	0.6	1	13.1	13.8	1.9	-48.2	21.9	-8.8	-12.8	28.3	0.6
	24		0.6	1	12.2	12.8	1.8	-45.2	22.9	-7.8	-10.6	30.2	0.7
	25		0.7	1	13.8	14.4	1.9	-50.1	21.2	-9.4	-13.3	27.9	0.6
	50	SC	0.4	1	8.9	9.6	1.5	-35.3	26.2	-4.6	-11.7	29.2	0.6
	47		0.4	1	8.6	9.3	1.4	-34.2	26.5	-4.3	-16.1	25.6	0.5
	49		0.5	1	10.8	11.4	1.6	-40.9	24.3	-6.4	-11.2	29.6	0.6
	42a		0.4	1	9.9	10.6	1.6	-38.3	25.1	-5.6	-9.4	31.1	0.7
	48		0.4	1	9	9.7	1.5	-35.6	26.1	-4.7	-8.7	31.7	0.7
	42e		0.3	1	8.4	9.1	1.4	-33.7	26.7	-4.1	-6.8	33.4	0.8
	51		0.4	1	9.5	10.2	1.5	-37	25.6	-5.2	-6.2	33.8	0.8

Continuation from Table 4.

Lithofacies	Sample Id	Facies	ln LN (fraction reacted)	a	10^6T2	Oxygen isotope fractionation $10^3 \times LN\ a$	Fraction reacted $\delta^{18}O$	δ pool ^{18}O	$\delta^{18}O$‰ (SMOW)	$\delta^{18}O$‰ (V-PDB)	$\delta^{13}C$‰ (V-PDB)	δ pool ^{13}C	Fraction reacted $\delta^{13}C$
Mound Structure	40		0.2	1	7.1	7.8	1.3	-29.6	28	-2.8	-19.8	22.5	0.4
	32		0.2	1	7.1	7.7	1.3	-29.5	28.1	-2.7	-10.2	30.5	0.7
	10		0.3	1	8.4	9	1.4	-33.5	26.7	-4	-11.2	29.6	0.6
	22		0.4	1	8.9	9.5	1.5	-35	26.2	-4.5	-14.4	27	0.6
	21		0.4	1	9.3	10	1.5	-36.4	25.8	-5	-14.4	27	0.6
	21b	gf-C	0.6	1	12.4	13.1	1.8	-46	22.6	-8.1	-13.9	27.4	0.6
	33		0.4	1	9.8	10.5	1.6	-38.1	25.2	-5.5	-12.1	28.9	0.6
	32c		0.3	1	8.4	9.1	1.4	-33.7	26.7	-4.1	-13.3	27.9	0.6
	46		0.5	1	10.1	10.8	1.6	-39	24.9	-5.8	-8.5	31.9	0.7
	41		0.2	1	7.1	7.8	1.3	-29.6	28	-2.8	-5.6	34.4	0.8
	45		0.4	1	9.7	10.4	1.5	-37.7	25.3	-5.4	-5.4	34.5	0.8
	44		0.5	1	10.2	10.8	1.6	-39	24.9	-5.8	-1.1	38.1	1
	11		0.2	1	6.2	6.9	1.2	-26.8	29	-1.9	-24	19	0.3
	11b		0.4	1	9.8	10.5	1.5	-38	25.3	-5.5	-18.8	23.3	0.4
	9a	fb-M	0.3	1	8.4	9	1.4	-33.5	26.8	-4	-18.5	23.6	0.4
	11a		0.3	1	8.4	9.1	1.4	-33.7	26.7	-4.1	-18	24	0.4
	11c		0.5	1	10.8	11.4	1.6	-41	24.3	-6.4	-9.9	30.8	0.7

Table 5. XRF Chemical composition and Fe, Ti, Al, and Mn ratios of representative samples of Cerro Matoso sediments.

Name	Sample Id	%										Index (Boström and Peterson, 1969)							
		SiO_2	Al_2O_3	Fe_2O_3	MgO	CaO	Na_2O	K_2O	TiO_2	P_2O_5	MnO	Al/ Al+Fe+Mn	100×Al/ (Al+Fe+Mn)	Al	Fe	Mn	Ti	Mn/Fe	Fe/Al	Fe/Ti
oil-C	43*	2.7	3.9	60.4	0.2	0.06	0	0	0	0.028	0.28	0.092	9.2	2.2	21.1	0.217	0	0.01	9.8	0
RC	cm-13	9.78	15.37	70.45	1.56	0.07	0.08	0	0.63	0.18	0.02	0.257	25.7	8.5	24.6	0.015	0.378	0.001	2.9	65.2
BM II	cm-19	8.92	5.31	79.27	1.81	0.08	0.08	0	0.05	0.01	1.02	0.094	9.4	2.9	27.7	0.79	0.03	0.028	9.4	925
Serp intr.	cm-20	23.05	4.82	67.31	1.75	0.13	0.08	0	0.05	0	1.29	0.098	9.8	2.7	23.5	0.999	0.03	0.042	8.8	785.5
CRC intr.	cm-27	19.87	4.47	71.25	1.75	0.08	0.08	0	0.04	0.12	0.58	0.089	8.9	2.5	24.9	0.449	0.024	0.018	10	1039.3
BM I	cm-25	12.42	2.52	76.17	1.63	0.17	0.08	0	0.03	0	5.87	0.043	4.3	1.4	26.6	4.547	0.018	0.171	19	1481.5
L	cm-14	27.54	4.24	61.89	2.39	0.25	0.08	0	0.05	0.03	0.86	0.095	9.5	2.4	21.6	0.666	0.03	0.031	9.2	722.2
GM	cm-9	33.88	10.63	39.13	4.03	5.67	1.27	0.08	0.47	3.15	0.16	0.3	30	5.9	13.7	0.124	0.282	0.009	2.3	48.6
bo-C	cm-11	22.25	17.4	53.86	2.45	0.09	0.08	0.01	0.73	0.17	0	0.339	33.9	9.7	18.8	0	0.438	0	1.9	43
gf-C	cm-5	10.83	8.94	72.35	4.52	0.4	0.08	0.01	0.36	0.1	0.55	0.162	16.2	5	25.3	0.426	0.216	0.017	5.1	117.3
fb-M	cm-1	18.39	6.71	65.81	5	0.44	0.08	0	0.16	0.06	0.56	0.137	13.7	3.7	23	0.434	0.096	0.019	6.2	240

Chemical composition of the main facies of the metal sediments obtained by x-ray fluorescence in Gmas laboratories. *Data taken from Gleeson *et al*. (2004). Black mudstone facies (BM I and BM II), red claystone (RC), orange iron laminated claystone (oil-C), listvenites (L), green intraclast (GC), red cemented intraclast (rc-C).

Table 6. ICP-MS analyses of tabular bed and mound structure sediments at Cerro Matoso (samples cm-19 and cm-26, cm-32, cm-35 and cm-43).

Analysis method	Detection limit	Analyzed element	Unit symbol	cm-19 BM II	cm-26 BM I	cm-32 gf-C	cm-35 Intra rc-C	cm-43 oil-C
TD-MS	0.01	Ca	%	0.03	0.06	0.15	0.07	0.02
INAA	0.01	Fe		46.1	38.4	36.8	41.9	36.5
TD-MS	0.01	Mg		0.66	0.72	2.05	0.53	0.25
INAA	0.01	Na		< 0.01	0.01	0.01	0.01	0.01
TD-MS	0.01	K		< 0.01	< 0.01	< 0.01	< 0.01	< 0.01
INAA	2	Au	ppb	< 2	< 2	< 2	< 2	< 2
TD-MS	10	Hg		< 10	130	10	< 10	< 10
MULT INAA/TD-ICP-MS	0.05	Ag	ppm	< 0.05	< 0.05	0.07	< 0.05	< 0.05
TD-MS	0.2	Cu		129	246	68.8	75.9	60.2
TD-MS	0.1	Cd		1	1.3	0.2	< 0.1	< 0.1
TD-MS	1	Mn		> 10000	> 10000	2870	5650	1590
TD-MS	0.5	Pb		< 0.5	0.5	4.5	< 0.5	1.8
MULT INAA/TD-ICP-MS	0.5	Ni		12500	14400	7170	11500	3160
MULT INAA/TD-ICP-MS	0.5	Zn		353	407	253	305	157
INAA	0.5	As		< 0.5	< 0.5	< 0.5	< 0.5	12.6
MULT INAA/TD-ICP-MS	1	Ba		7	12	13	14	3
TD-MS	0.1	Be		0.8	2.3	0.7	0.6	0.3
TD-MS	0.02	Bi		< 0.02	0.03	0.22	< 0.02	0.49
INAA	0.5	Br		< 0.5	< 0.5	< 0.5	< 0.5	< 0.5
MULT INAA/TD-ICP-MS	0.1	Co		2600	3040	282	385	37.2
INAA	2	Cr		9670	17500	15300	23500	13800
MULT INAA/TD-ICP-MS	0.05	Cs		< 0.05	< 0.05	< 0.05	< 0.05	< 0.05
INAA	1	Hf		< 1	< 1	< 1	< 1	2
TD-MS	0.1	Ga		4.2	4.8	13.2	3.9	23.8
TD-MS	0.1	Ge		1	0.6	0.4	0.4	0.3
TD-MS	0.1	In		< 0.1	< 0.1	< 0.1	< 0.1	0.2
TD-MS	0.5	Li		0.9	1	10.9	< 0.5	10.7
TD-MS	0.1	Nb		< 0.1	< 0.1	2.6	< 0.1	4.6
TD-MS	0.05	Mo		1.13	1.44	1.14	0.79	3.97
TD-MS	0.2	Rb		< 0.2	< 0.2	< 0.2	0.3	< 0.2

Continuation from Table 6.

Analysis method	Detection limit	Analyzed element	Unit symbol	cm-19 BM II	cm-26 BM I	cm-32 gf-C	cm-35 Intra rc-C	cm-43 oil-C
TD-MS	0.001	Re		< 0.001	< 0.001	< 0.001	< 0.001	< 0.001
INAA	0.1	Sb		< 0.1	< 0.1	< 0.1	< 0.1	1
INAA	0.1	Sc		39.3	55.7	48	46.1	58.3
MULT INAA/TD-ICP-MS	0.1	Se		0.2	0.6	2.4	2.4	2.7
TD-MS	1	Sn		< 1	< 1	< 1	< 1	2
TD-MS	0.2	Sr		1	2.4	3.1	2.7	1.9
MULT INAA/TD-ICP-MS	0.1	Ta		< 0.1	< 0.1	0.2	< 0.1	0.4
TD-MS	0.1	Te		0.2	0.3	0.3	< 0.1	0.7
MULT INAA/TD-ICP-MS	0.1	Th		< 0.1	< 0.1	2.2	< 0.1	4.3
TD-MS	0.05	Tl		0.05	< 0.05	< 0.05	< 0.05	< 0.05
MULT INAA/TD-ICP-MS	0.1	U		< 0.1	< 0.1	0.7	< 0.1	1.7
TD-MS	1	V		89	716	82	25	160
TD-MS	1	Zr		2	3	48	2	77
INAA	1	W		< 1	< 1	< 1	< 1	< 1
TD-MS	0.1	Y		10.7	17.7	4.6	3	1.7
TD-MS	0.1	La		11.5	10.3	3.9	4	3.1
TD-MS	0.1	Ce		0.1	0.1	8.6	35.2	5.2
TD-MS	0.1	Pr		5.6	8.3	1.2	1.1	0.8
TD-MS	0.1	Nd		24.4	35.5	5	4.7	2.9
TD-MS	0.1	Sm		6.3	9.9	1.2	1.2	0.6
TD-MS	0.05	Eu		1.7	3.02	0.29	0.33	0.1
TD-MS	0.1	Gd		4.4	8	1.1	0.9	0.4
TD-MS	0.1	Tb		0.7	1.6	0.1	0.1	< 0.1
TD-MS	0.1	Dy		4.5	10.7	1	0.9	0.3
TD-MS	0.1	Ho		0.8	2	0.2	0.2	< 0.1
TD-MS	0.1	Er		2.4	6.5	0.7	0.5	0.3
TD-MS	0.1	Tm		0.4	1.1	0.1	< 0.1	< 0.1
TD-MS	0.1	Yb		2.7	8.3	0.8	0.9	0.4
TD-MS	0.1	Lu		0.4	1.2	0.1	0.1	< 0.1
INAA	0	Mass	g	1.01	0.745	0.981	0.583	0.91

Note: W, U, Th, Ta, Sb, Sn, Re, Rb, Nb, In, Hf, Cs, Br, As are under the detection limit.

Table 7. Equation form elements normalization of Cerro Matoso (samples cm-19 and cm-26, cm-32, cm-35 and cm-43).

Equations of normalization	cm-19 BM II	cm-26 BM I	cm-32 gf-C	cm-35 Intra rc-C	cm-43 oil-C
Ce anom= log (Ce/(2/3La + 1/3Nd))	-2.52225	-2.59931	-0.01508	0.60106	-0.083
Eu anom= 2Eu/(Sm + Gd) normalizad PAAS?	1.37764	1.45418	1.08109	1.35861	0.86874
(LaSN/YbSN)	0.36671	0.10684	0.41973	0.38266	0.66726
LaSN/SmSN	0.33391	0.19032	0.59451	0.60976	0.94512
>1 en MORB-E, LaSN/PrSN	0.50588	0.3057	0.80061	0.89579	0.95457
EuSN/GdSN	1.52386	1.4889	1.03981	1.44617	0.98602
DySN/HoSN	1.76863	1.25677	1.20683	1.37329	-

Discussion

Previous work has shown that the assemblage of berthierine/greenalite + siderite crystallization can be associated with formation conditions consistent with high temperatures, alkaline pH, and reducing environments that characterize deep-sea hydrothermal systems, even the Fe-Mn oxyhydroxides have a clear hydrothermal origin (*e.g.,* Dias and Barriga, 2006; Dias *et al*., 2011). Fissured and brecciated appearances in the sediments accompanied by a network of microcracks, open and common ducts, and high porosity, with vug and mold porosity, have been associated with the exhalation of fluids. The formation of these sedimentary structures is therefore analogous to fluid-induced chimney formation on the modern ocean floor (*e.g.,* Eickmann *et al*., 2021). Although the marine sediments of the upper parts of the oceanic crust accreted to the continent are usually not preserved, the black color and mineral content of the tabular succession plus the fossil content in both successions do not fit with humid tropical conditions of oxidation of peridotites that generate red laterites. Therefore, serpentinization-derived fluids involved in the formation of the mound structures, conduit-filling cement, and tabular bed succession can be supported by these novel data.

The element and stable isotope composition of the sedimentary succession have been used to reconstruct the origin and nature of the fluids from which they are formed. In this sense oxygen, and carbon isotope values of the bulk sediments from Cerro Matoso are consistent with those observed in serpentinization settings of ultramafic rocks (*e.g.,* Lavoie and Chi, 2010; Lartaud *et al*., 2011; Klein *et al*., 2015; Eickmann *et al*., 2021). Although most of the $\delta^{18}O$ values of the gf-C facies are in the range of surface temperatures considering meteoric water (Figure 9), which is supported by the relatively negative $\delta^{13}C$ values, samples 32 and 41 present $\delta^{18}O$ values indicating temperatures close to 80ºC. Samples of siderite concretions SC are in the same range. The isotopic composition of smectites produced by ultramafic weathering (Savin and Epstein, 1970), with $\delta^{18}O$ values (20.3 to 24.3‰ SMOW), in the nickel smectites in Murrin Murrin, Western Australia, represent water-rock interactions at low temperatures due to the contact of meteoric fluids during mineral leaching processes in which laterites are formed (Gaudin *et al*., 2005). This data show consistency with most of the Cerro Matoso isotope data. Although, marine water or diagenetic fluid relatively enriched in ^{18}O (>–3‰ *vs* V-SMOW) could explain the temperatures above 50 degrees of samples 32 and 41, a maximum temperature of approximately 90°C, considering meteoric waters are reported in low latitudes close to –4‰ (V-SMOW). Nevertheless, the Ni-laterites formed by supergene alterations of peridotites is a relatively recent process at which the environmental temperatures do not exceed 50°C. Additionally, the wider range of $\delta^{18}O$ value (15.9 to 29.8‰ V-SMOW), of the tabular succession also could be explained by surficial temperatures or low temperature hydrothermal/diagenetic system, which fit with the negative $\delta^{13}C$ values (–21.6 to –8.1‰ V-PDB) that are compatible with meteoric waters. However, samples corresponding to the BM II facies and their intraclasts report lower values of $\delta^{18}O$ (25.1 to 29.8‰ SMOW). These higher temperatures are only justified if fluids are enriched in ^{18}O (magmatic, metamorphic, or diagenetic water).

The lower $\delta^{13}C$ values (in intraclast, –27‰ V-PDB) could only be explained by these processes or by the oxidation of methane related to these systems. According to Irwin *et al*. (1977), marine/diagenetic waters with relatively negative values of Dissolved Inorganic Carbon (DIC) are formed by the biological degradation of organic matter in closed systems. However, there is no obvious source of significant organic material (*e.g.,* carbon-rich shales) in the sedimentary succession hosting the Cerro Matoso peridotites, so there must be another source of isotopically light DIC. We suggest the production of abiogenic methane by serpentinization of peridotite as

the light $\delta^{13}C$ source. Methane in modern serpentinite-derived fluids in both the deep-sea and ophiolite environments have negative $\delta^{13}C$ values (*e.g.,* –18‰ at Elba and –7.7‰ in the Zambales ophiolite; –16.7‰ at Rainbow; –10.3‰ at Logatchev; –11.9‰ at Lost City; Abrajano *et al*., 1988; Lilley *et al*., 1993; Charlou *et al*., 2002; Proskurowski *et al*., 2008a; Meister *et al*., 2018; Sciarra *et al*., 2019; Eickmann *et al.,* 2021). Part of this methane will be oxidized close to the seafloor to produce ^{13}C-depleted DIC, and high pH and Ca concentrations in the serpentinite-derived fluids trigger carbonate and mineral precipitation on mixing with seawater (Palandri and Reed, 2004; Proskurowski *et al*., 2008b). The fluids generated during the peridotite serpentinización favored the calcareous sedimentary succession formations on top of the crystalline rocks when these rocks were exposed at a mid-oceanic ridge (Figure 11). Calcareous intraclasts (Id 1, 2, 5, and 35) within the BM II facies, with $\delta^{13}C$ values between –27.1 and –17.1‰, indicate a low contribution of marine DIC surely associated with the anaerobic oxidation of methane process (AOM). In this sense, the carbon isotopic composition of Thyasira aff. southwardae shells from "Clamstone" site on Rainbow Hill, with signatures of more depleted ^{13}C ($\delta^{13}C$ = −7.69±1.60‰) than expected, is interpreted as a contribution of oxidized methane in the pore-water filling the burrows formed by the bivalves (Lartaud *et al*., 2010). Our C-isotope data are in the range of serpentinite samples of six different regions in the Mid Atlantic Ridge (MAR) yielded $\delta^{13}C$ values ranging from –29 to –4‰ (Früh-Green *et al.,* 2004), which sign methane sources. The rare rock fragments characterized by altered ultramafic lithoclasts (serpentinites) and claystone, are in part similar to those described by Dias and Barriga (2006) for Saldanha sediments, a hydrothermal site of the MAR partly supported by serpentinization processes. According to Lartaud *et al.* (2011), owing to the very low concentration of inorganic carbon in serpentinization fluids, the most feasible origin for this ^{13}C depleted is the oxidation of methane.

Although recently clumped isotope thermometry could constrain the temperature ranges of the carbonates and clays, the carbon isotope data in Cerro Matoso agree in part with the values of $\delta^{13}C$ of CH_4 and CO_2 of high and low-temperature hydrothermal fluids, at 9°50´N East Pacific Rise, with an average value of $\delta^{13}C$ of –30.2±2.7‰ and –4.5±0.53‰, respectively, which are somewhat more diminished than the average values of $\delta^{13}C$ in high-temperature vents, –20.1±1.2‰ of CH_4 and –4.08 of CO_2 (Proskurowski *et al*., 2008b). These values are among the lightest measured in hydrothermal vents (Lilley *et al*., 1993; Shank *et al*., 1998; Charlou *et al*., 1998, 2002). In general, carbon dioxide is derived from magmatic degassing, which retains values of $\delta^{13}C$, mainly between –4 and –8‰ (Campbell and Larson, 1998), and carbonates in the mantle, between –5 and –7‰ (Alt *et al*., 1986; Hoefs and Sywall, 1997), will be related only to the most negative $\delta^{13}C$ isotopic signature of the marine sediments in Cerro Matoso because in general, all samples present a wide range of $\delta^{13}C$. The more negative $\delta^{13}C$ values in Cerro Matoso samples point out the presence of methane oxidation events, favoring the growth of carbonates in the sediments overlying the ultramafic rocks. Similar conditions have been reported around deep marine hydrothermal vents by Kelley *et al*. (2001), Früh-Green *et al*. (2004), and Eickmann *et al*. (2021).

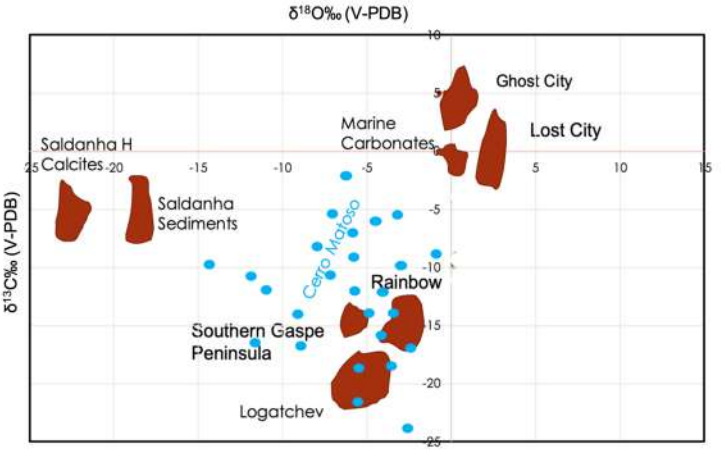

Figure 11. $\delta^{13}C$ (V-PDB) *vs* $\delta^{18}O$ (V-PDB) from Cerro Matoso hydrothermal sediments. For comparison, hydrothermal calcite values associated with mineral formation in hydrothermal systems at Lost City (Klein *et al*., 2015), Saldanha sediments (Dias *et al*., 2011), carbonates at Ghost City (Lartaud *et al*., 2011), carbonates and brecciated serpentinites to the south of the Gaspe Peninsula (Lavoie and Chi, 2010); and hydrothermal fluids at Rainbow and Logatchev (Charlou *et al*., 2002).

The initial isotopic carbon ratio of the carbon dioxide discharged from geothermal and ultramafic systems in oceanic ridges, ranges from –8‰ to –3‰, plus the maximum fractionation factor resulting from the oxidation of anaerobic or aerobic methane (1.039) at hydrothermal environments around ultramafic rocks (Whiticar and Faber, 1986; Proskurowski *et al.,* 2008b), could favor a depletion by at least –13‰ of the original isotope signature, giving $\delta^{13}C$ values around –21‰ that are consistent with the negative isotopic signature of the minerals forming marine claystone and mudstone in Cerro Matoso. Although the less depleted $\delta^{13}C$ values are in the range of meteoric siderite line (MSL) (Figure 8) that could reflect biological processes related to the degradation of organic matter, these values may also record anaerobic oxidation of methane or bacterial oxidation/sulfate-reduction (Irwin *et al*., 1977). The ancient hydrothermal activity in the Cerro Matoso peridotites is supported by the identification of listvenites (Castrillón and Guerrero, 2020), precisely rocks that are underlying the Fe-rich mudstone succession. If this interpretation is correct, then it suggests that serpentinization-derived fluids flow was active for a considerable time according to the mounds and tabular unit thickness, as well as during the formation of listvenites, and this process was localized in the north area of the Cerro Matoso peridotites.

Geochemical analyses of the sediments show that are associated with high-temperature (*i.e.,* Fe, Cu, Zn, and Ba) but also in elements usually related to hydrothermal low-temperature (Mn), and metasomatism (Mg) in areas where mantle rocks host hydrothermal systems. According to the chemical composition of claystone and mudstone succession, both can be differentiated as hydrothermal or metalliferous sediments. The high iron content of the tabular succession (>80%) plus Cu and Zn permits us to consider it as metalliferous sediments (*e.g.,* Mills and Elderfield, 1995a; Dekov *et al.,* 2010). Additionally, the criteria of Mn/Fe, Fe/Al and Fe/Ti ratios used to identify metalliferous sediments (*e.g.,* Bonatti, 1981; Peter and Goodfellow, 1996; Dekov *et al*., 2010) indicate that the claystone is in the range of hydrothermal systems and mudstones correspond to metalliferous sediments, respectively. The later, with Mn/Fe > 0.28, Fe/Al > 9.4, and Fe/Ti > 925 ratios *vs* Mn/Fe < 0.019, Fe/Al < 6.2, and Fe/Ti < 240 from the claystone facies, also indicate their different origin (Table 5). In general, Dias *et al*. (2011) suggest that hydrothermal phases derived from low-temperature hydrothermal fluids are characterized by Mn and Fe oxyhydroxides and minor amounts of sulphide precipitates, whereas high-temperature fluids favor precipitation of Cu-sulfides at depth, followed by Cu-Zn and Fe sulfides, which are furthermore characteristic of deep-sea hydrothermal systems. The Al/Al + Fe + Mn has been used to identify the contribution of pelagic sediments to deep marine sediments (*e.g.,* Bonatti, 1981; Dekov *et al.,* 2010). The ratio <0.4 of the Cerro Matoso sediments indicates no contribution of sediments from a continent scenario, which is consistent with the idea of a deep-sea hydrothermal origin instead of a supergene one. In this case, the origin of the metals enrichment could be explained by a plume fall-out source located in an ancient hydrothermal system in the mid-ocean Pacific ridge, where the peridotites were exhumed. The hydrothermal contribution against a detrital in marine sediments has also been estimated using Fe/Ti *vs* Al/(Al + Fe + Mn) relation (after Boström and Peterson, 1969; Peter and Goodfellow, 1996) in where Dekov *et al.* (2010) indicate that all hydrothermal sediments must be on a theoretical curve (Figure 12), in which a Fe/Ti ratio decreasing and Al/(Al + Fe + Mn) increasing sign a dilution of metal sediments with pelagic deep-sea sediments.

A negative Ce (Ce/Ce* = –2.52 to –2.59) anomaly and a positive Eu (Eu/Eu* = 1.37 to 1.45) anomaly that characterize the Cerro Matoso black mudstone sediments have a similar REE pattern of some hydrothermal fluids (*e.g.,* Rainbow's hydrothermal sediments and transatlantic Geotraversa (TAG), James *et al*., 1995; Douville *et al*., 1999, 2002; Dias and Barriga, 2006) (Figure 13). A very high positive Eu anomaly is also marked in many hydrothermal phases (*e.g.,* Fe oxyhydroxides with sulfates and sulphide) derivatives of these fluids (*e.g.,* Mills *et al.,* 1993; Mills and Elderfield, 1995a; German *et al*., 1999). On the other side, the pattern of Ce negative anomalies and LREE enrichment characteristic of marine waters (Elderfield, 1988), definitely associate the mudstones with marine environments.

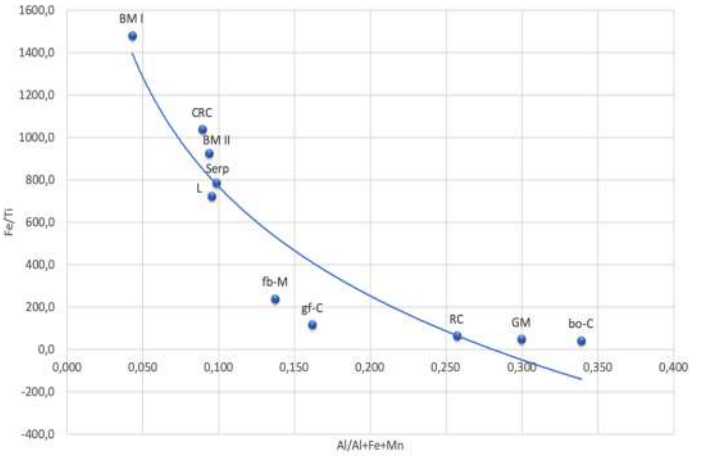

Figure 12. Fe/Ti ratio *vs* Al/(Al + Fe + Mn) for the sediments of Cerro Matoso which matches the pattern presented by the metalliferous sediments of the Eastern Pacific Dorsa, EPR (adapted from Boström and Peterson, 1969). fb-M: cracked and breached mudstone, gf-C: fossiliferous green claystone, bo-C: brown oxidized claystone, BM I and BM II: black mudstone I and II, RC: red claystone, L: Listvenites, GM: green mudstone, rc-C: red intraclast, Serp: serpentinite intraclast.

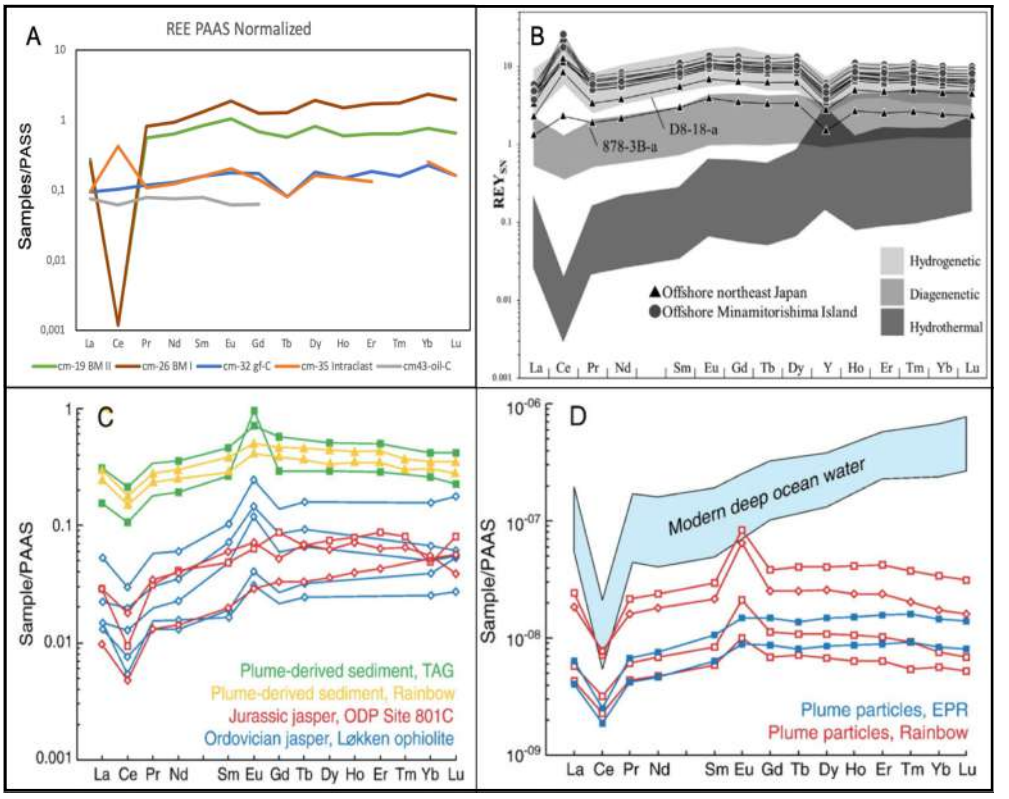

Figure 13. A. PAAS normalized REE patterns of Cerro Matoso sediments: Black mudstone I and II (BM I and BM II), intraclast (rc-C), fossiliferous green claystone (gf-C), orange iron laminated claystone (oil-C). **B.** Shale-normalized REY spider diagram for the Fe-Mn crusts. Hydrogenetic (Hein *et al*., 2012), diagenetic (Bau *et al*., 2014), and hydrothermal (Bau *et al.,* 2014) REY data fields are also plotted. **C.** Hydrothermal plume-derived iron oxide sediment from the TAG hydrothermal field, Mid-Atlantic Ridge (German *et al.,* 1993) and the Rainbow vent field of the Mid-Atlantic Ridge (Chavagnac *et al*., 2005), Ordovician jasper from the Løkken district, Norway (Grenne and Slack, 2003, 2005), and Jurassic jasper from ODP Site 801C (Alt *et al*., 2003) in the western Pacific Ocean (unpublished ICP-MS data of O.J.R.). **D.** Modern deep ocean water (Byrne *et al*., 1996), and hydrothermal plume particles from the Rainbow vent field of the Mid-Atlantic Ridge (Edmonds and German, 2004) and the East Pacific Rise at 9°45′N (Sherrell *et al*., 1999). PAAS data from McLennan (1989) and C, D, modified from Slack *et al*. (2007).

Hongo *et al*. (2007) consider that both anomalies indicate a dilution of a hydrothermal fluid signature and removal activity of ocean water particles, reported in mid-ocean ridges. A marked depletion in Ce relative to Pr and La (Shale-normalized patterns) reported here are similar to metalliferous sediments at the EPR, characterized by Bender *et al*. (1971) with a distinct enrichment in the heavy REE (HREE) relative to the light REE (LREE) (Piper and Graef, 1974; Marchig *et al*., 1982). Rare earth elements (REE) concentrations are low and PAAS-normalized patterns are characteristic of high-temperature vent fluids with enrichment in light REE and a pronounced positive Eu anomaly (Dias *et al.,* 2011). The REE pattern could be compared with those of iron formations or BIFs (Archean and Early Proterozoic), characterized by high light REE/heavy REE ratios and positive Eu anomalies, which have been interpreted as reflecting hydrothermal sources in mid-oceanic ridges (MOR) (Beukes and Klein, 1990; Bau and Dulski, 1999; Johnson *et al*., 2003). Barrett and Jarvis (1988), indicate that the seawater-like pattern of EPR sediments can result from the rapid precipitation and adsorption of seawater REE onto hydrothermally derived Fe-Mn-oxyhydroxide colloidal particles after the particles have settled onto the sea floor or even in the water column. In this sense, Klinkhammer *et al*. (1983) infer that LREE are removed from the seawater by hydrothermal circulation. The different LREE depletion degrees between samples cm-19 and cm-26 can be interpreted as an effect of the initial reaction that removed LREE from the seawater. These reactions preferentially remove LREE from sea water, leaving the reacted (or scavenged) seawater of the plume even more LREE depleted (Klinkhammer *et al.,* 1983). But also mean a continued post-depositional diagenetic reaction that can involve scavenging from pore water which may increase the proportion of LREE to HREE in the sediment (Barrett and Jarvis, 1988). Additionally, REE/Fe ratios of the BM I (3.3×10^{-4}) and BM II (1.7×10^{-4}) facies are quite similar to REE/Fe ratios of Rainbow hydrothermal field particles (REE/Fe = 1.6×10^{-4}) (Chavagnac *et al.,* 2005).

Considerable variation in REE concentration in the black mudstone facies could indicate the existence of a hydrothermal plume that contained many suspended metals, which sequestered rare earth elements (REE) from ocean water and then precipitated within the mudstone. On the other side, the high carbonate concentration in the samples cm-19 and cm-26 suggests that fluid REE fractionation could be induced by coprecipitation with hydrothermally originated minerals (*e.g.,* carbonate), and later by adhesive removal by Fe and/or Mn oxide particles. At any case, REE corroborates that metal sediments inherit their REE signature from deep-sea waters where they precipitate (Dubinin, 2004), and are evidence that claystone and mudstone at Cerro Matoso Pit-1 were formed in a deep-marine setting.

A positive Ce anomaly of Ce of intraclasts (rc-C) (*i.e*., sample cm-35), corresponds to an anomaly related to a hydrogenic origin (Azami *et al*., 2018) or according to Tostevin *et al*. (2016), could represent deep-sea Fe-Mn crust. Positive Ce anomaly characterizing the intraclasts into BM II facies indicates that the marine sediments could have slumped during the hydrothermal activity and could be the oldest rocks in the deposits, which is consistent with their relationship in the field. Indeed, except for Ce anomalies, the patterns are similar to those of modern plume-related iron oxyhydroxide particles and sediments as well as Phanerozoic hydrothermal sediments (Slack *et al*., 2007). Slack *et al.* (2007), compare the range of anomalies with those of oxide particles in the buoyant (near-vent) and non-buoyant (more distal) parts of modern plumes that are consistent with a model of increasing dilution of hydrothermal fluids by ambient seawater away from vents, with dilution factors on the order of 10^4 in non-buoyant plume (*e.g.,* German *et al.,* 1993; German and Von Damm, 2003). McMurtry and Burnett (1975) suggest that this kind of sediments unusually enriched with iron, manganese, and other metals, are correlated with areas of high heat flow on oceanic ridges where circulate hydrothermal fluids are generated during mid-oceanic rift volcanism.

The geochemical analysis suggests that a deep-sea hydrothermal activity hosted by the ultramafic rocks favored the mantle rocks serpentinization and contributed to the formations of a thick sedimentary succession associated with biological process and the plume vent fall-out depending on the Eh/pH water changes (Figure 14). The peridotites and marine mudstone/claystone were attached to the continent where the full set of rocks suffered the supergene leaching process allowing the nickel laterite formation as we know today. These explain the differences between Cerro Matoso deposit with other nickel laterites in the Caribbean.

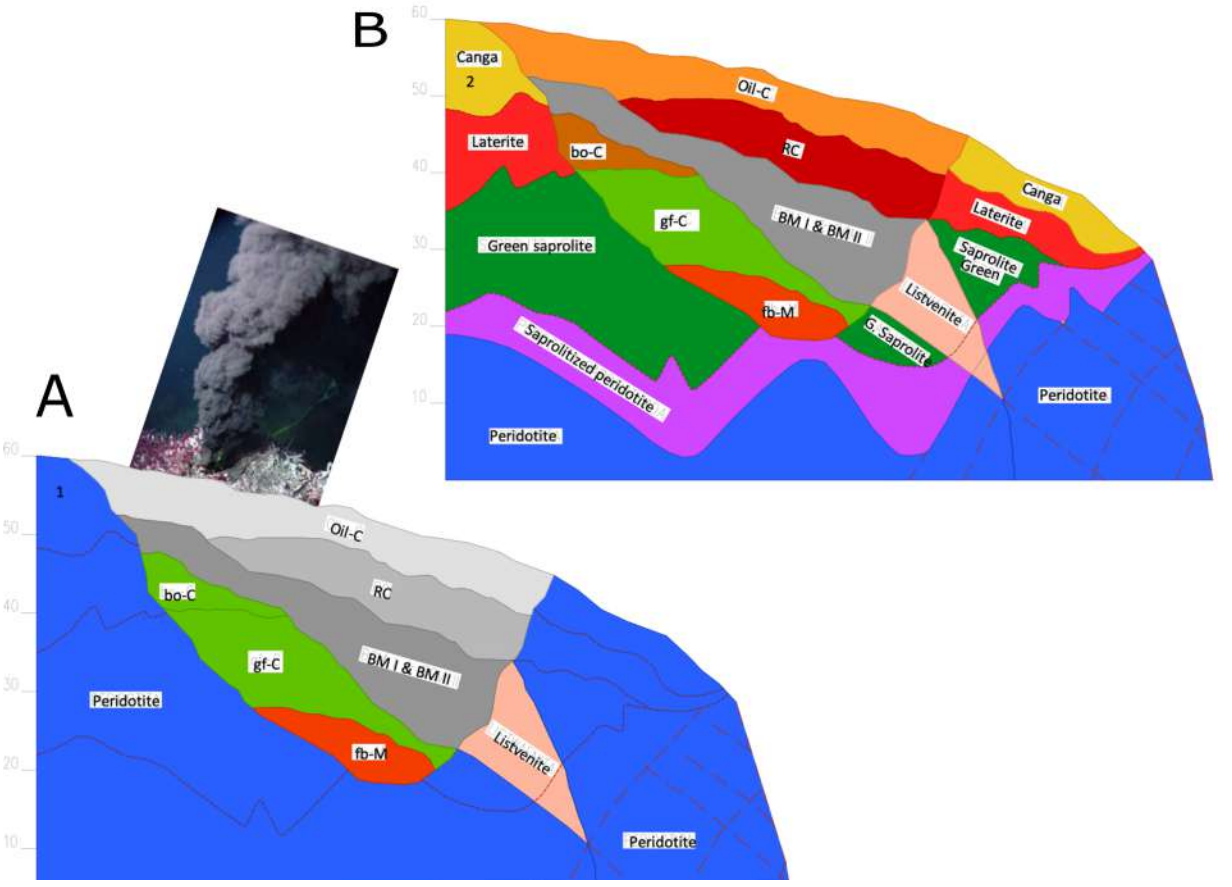

Figure 14. A. Deep-sea ultramafic rock hosting a hydrothermal system where mudstone and claystone were formed. **B.** Cerro Matoso laterite profile after intense supergene leaching. fb-M: cracked and breached mudstone, gf-C: fossiliferous green claystone, bo-C: brown oxidized claystone, BM I and BM II: black mudstone I and II, RC: red claystone, oil-C: orange iron laminated claystone, L: Listvenites.

Conclusions

The Cerro Matoso sediments, can be understood as ancient examples of a carbonate mineralized seafloor feature that are formed from serpentinization-related seepage in deep-marine settings. $\delta^{18}O$ values and temperature-dependent relations (*i.e.,* reaching 130ºC) that present the black mudstone succession indicate precipitation related to a low-temperature hydrothermal fluids influence. The REE patterns, Eu positive and Ce negative anomaly suggest precipitation of a hydrothermal plume fall-out as a source of the black mudstone facies and their hydrothermal phases (oxyhydroxides and silicates) which fit with a serpentinization-derived fluid affecting the mantle rocks of Cerro Matoso. The negative $\delta^{13}C$ values confirm deep marine environments in which isotopically light carbon is released from methane and organic matter microbial entry. The very negative CO_2 generated contributes to lower the residual isotopic $\delta^{13}C$ values of marine waters. The Fe/Ti *vs* Al/(Al + Fe + Mn) ratios and maximum Al/(Al + Fe + Mn) ratio (<0.4) point out that the Cerro Matoso mantle rocks proceed from the Pacific mid-ocean ridge, where hosted hydrothermal vent plumes responsible for the enrichment of associated metals.

Acknowledgments

This paper shows part of the Doctoral dissertation of the first author (A. Castrillón), who gratefully acknowledges a fellowship from Colciencias (National Doctorate, scholarship 647) and Universidad Nacional de Colombia. Isotope analyses were done in the Instituto Andaluz de Ciencias de la Tierra, Granada, Spain. The authors express their gratitude to Dr. Dario Barrero, for his comments, and to Dr. Brian Fry for his selfless collaboration and valuable contributions to isotope modeling, and thanks to Cerro Matoso. This work also was possible thanks to the support of Dr. Augusto Rodriguez and the Instituto de Geología and Instituto

de Geofísica Ambiental from the Universidad Nacional Autónoma de México. Datasets for this research are included in this paper and supplementary information files can be found in. Castrillón, Andres (2020), "Open systems fractionation factor CM", Mendeley Data, v1. https://doi.org/10.17632/8fr82mx34x.1#file-51080efe-3098-4796-a5ae-384707ae2ddb

References

Abrajano, T.A.; Sturchio, N.C.; Bohlke, J.K.; Lyon, G.L.; Poreda, R.J.; Stevens, C.M. (1988). Methane-hydrogen gas seeps, Zambales ophiolite, Philippines: Deep or shallow origin? *Chemical Geology, 71*(1-3), 211-222. https://doi.org/10.1016/0009-2541(88)90116-7

Agrinier, P.; Hékinian, R.; Bideau, D.; Javoy, M. (1995). O and H stable isotope compositions of oceanic crust and upper mantle rocks exposed in the Hess Deep near the Galapagos Triple Junction. *Earth and Planetary Science Letters, 136*(3-4), 183-196. https://doi.org/10.1016/0012-821X(95)00159-A

Al-Aasm, I.S.; Taylor, B.E.; South, B. (1990). Stable isotope analysis of multiple carbonate samples using selective acid extraction. *Chemical Geology: Isotope Geoscience Section*, *80*(2), 119-125. https://doi.org/10.1016/0168-9622(90)90020-D

Alt, J.; Muehlenbachs, K.; Honnorez, J. (1986). An oxygen isotopic profile through the upper kilometer of the oceanic crust, DSDP Hole 504B. *Earth and Planetary Science Letters, 80*(3-4), 217-229. https://doi.org/10.1016/0012-821X(86)90106-8

Alt, J.C.; Shanks III, W.C. (1998). Sulfur in serpentinized oceanic peridotites: Serpentinization processes and microbial sulfate reduction. *Journal of Geophysical Research: Solid Earth, 103*(B5), 9917-9929. https://doi.org/10.1029/98JB00576

Alt, J.C.; Teagle, D.A.H. (2003). Hydrothermal alteration of upper oceanic crust formed at a fast-spreading ridge: mineral, chemical, and isotopic evidence from ODP Site 801. *Chemical Geology, 201*(3-4), 191-211. https://doi.org/10.1016/S0009-2541(03)00201-8

Alt, J.C.; Shanks III, W.C.; Bach, W.; Paulick, H.; Garrido, C.J.; Beaudoin, G. (2007). Hydrothermal alteration and microbial sulfate reduction in peridotite and gabbro exposed by detachment faulting at the Mid-Atlantic Ridge, 15°20´N (ODP Leg 209): A sulfur and oxygen isotope study. *Geochemistry, Geophisys, Geosystems, 8*(8). https://doi.org/10.1029/2007GC001617

Azami, K.; Hirano, N.; Machida, S.; Yasukawa, K.; Kato, Y. (2018). Rare earth elements and yttrium (REY) variability with water depth in hydrogenetic ferromanganese crust. *Chemical Geology, 493*, 224-233. https://doi.org/10.1016/j.chemgeo.2018.05.045

Barrero, D. (1974). Metamorfismo regional en el Occidente Colombiano. *Simposio sobre ofiolitas Medellín*, Colombia, Medellín.

Barrett, T.J.; Jarvis, I. (1988). Rare-earth element geochemistry of metalliferous sediments from DSDP Leg 92: The East Pacific Rise transect. *Chemical Geology*, *67*(3-4), 243-259. https://doi.org/10.1016/0009-2541(88)90131-3

Bau, M.; Dulski, P. (1999). Comparing yttrium and rare earths in hydrothermal fluids from the Mid-Atlantic Ridge: implications for Y and REE behavior during near-vent mixing and for the Y/Ho ratio of Proteozoic seawater. *Chemical Geology, 155*(1-2), 77-90. https://doi.org/10.1016/S0009-2541(98)00142-9

Bau, M.; Schmidt, K.; Koschinsky, A.; Hein, J.; Kuhn, T.; Usui, A. (2014). Discriminating between different genetic types of marine ferro-manganese crusts and nodules based on rare earth elements and yttrium. *Chemical Geology*, *381*, 1-9. https://doi.org/10.1016/j.chemgeo.2014.05.004

Bender, M.L.; Broecker, W.; Gornitz, V.; Middel, U.; Kay, R.; Sun, S.S.; Biscaye, P. (1971). Geochemistry of three cores from the East Pacific Rise. *Earth and Planetary Science Letters, 12*(4), 425-433. https://doi.org/10.1016/0012-821X(71)90028-8

Beukes, N.; Klein, C. (1990). Geochemistry and sedimentology of a facies transition - from microbanded to granular iron formartion - in the early Proterozoic Transvaal Supergroup, South Africa. *Precambrian Research*, *47*(1-2), 99-139. https://doi.org/10.1016/0301-9268(90)90033-M

Bonatti, E. (1981). Metal deposits in the oceanic lithosphere. In: C. Emiliani (ed.). *The Sea* (pp. 639-686). vol. 7. John Willey and Sons.

Boström, K.; Peterson, M. (1969). The origin of aluminium-poor ferromanganoan sediments in areas of high heat flow on the East Pacific Rise. *Marine Geology, 7*(5), 427-447. https://doi.org/10.1016/0025-3227(69)90016-4

Byrne, R.H.; Sholkovitz, E.R. (1996). Marine chemistry and geochemistry of the lanthanides. *Handbook on the Physics and Chemistry of Rare Earths*, *23*, 497-593, https://doi.org/10.1016/S0168-1273(96)23009-0

Byrne, R.H.; Liu, X.; Schijf, J. (1996). The influence of phosphate coprecipitation on rare earth distributions in natural waters. *Geochimica et Cosmochimica Acta, 60*(17), 3341-3346, https://doi.org/10.1016/0016-7037(96)00197-4

Campbell, A.C.; Palmer, M.R.; Klinkhammer, G.P.; Bowers, T.S.; Edmond, J.M.; Lawrence, J.R.; Casey, J.F.; Thompson, G.; Humphris, S.; Rona, P.; Karson, J.A. (1988). Chemistry of hot springs on the Mid-Atlantic Ridge. *Nature, 335*(6190), 514-519. https://doi.org/10.1038/335514a0

Campbell, A.R.; Larson, P.B. (1998). Introduction to stable isotope applications in hydrothermal systems. In: J.P. Richards, P.B. Larson (eds.). *Techniques in Hydrothermal Ore Deposits Geology*. Society of Economic Geologists. https://doi.org/10.5382/Rev.10.08

Carothers, W.W.; Adami, L.H.; Rosenbauer, R.J. (1988). Experimental oxygen isotope fractionation between siderite-water and phosphoric acid liberated CO_2-siderite. *Geochimica et Cosmochimica Acta, 52*(10), 2445-2450. https://doi.org/10.1016/0016-7037(88)90302-X

Castrillón, A. (2019). Carbonatos y otros minerales autigénicos asociados a las lateritas niquelíferas de Cerro Matoso y su posible relación con actividad hidrotermal y reducción de sulfatos. Ph.D. Thesis, Universidad Nacional de Colombia, Bogotá, Colombia.

Castrillón, A.; Guerrero, J. (2020). Listvenites: new insights of a hydrothermal system fossilized in Cerro Matoso peridotites, Montelíbano, Córdoba Department, Colombia. *Boletín Geológico, 47*, 67-84. https://doi.org/10.32685/0120-1425/boletingeo.47.2020.492

Castrillón, A.; Pi-Puig, T.; Guerrero, J.; Nuñez-Useche, F.; Rodriguez, A.; Canet, C. (2022). Clay mineralogy and texture of deep-sea hydrothermal mudstone associated with the Cerro Matoso peridotite in accreted oceanic crust from Colombia. *Journal of South American Earth Sciences, 117,* 103886. https://doi.org/10.1016/j.jsames.2022.103886

Charlou, J.; Fouquet, Y.; Bougault, H.; Donval, J.; Etoubleau, J.; Jean-Baptiste, P.; Dapoigny, A.; Appriou, P.; Rona, P. (1998). Intense CH_4 plumes generated by serpentinization of ultramafic rocks at the intersection of the 15º20´N fracture zone and the Mid-Atlantic Ridge. *Geochimica et Cosmochimica Acta, 62*(13), 2323-2333. https://doi.org/10.1016/S0016-7037(98)00138-0

Charlou, J.L.; Donval, J.P.; Fouquet, Y.; Jean-Baptiste, P.; Holm, N. (2002). Geochemistry of high H_2 and CH_4 vent fluids issuing from ultramafic rocks at the Rainbow hydrothermal field (36°14′N, MAR). *Chemical Geology, 191*(4), 345-359. https://doi.org/10.1016/S0009-2541(02)00134-1

Chavagnac, V.; German, C.; Milton, J.; Palmer, M. (2005). Sources of REE in sediment cores from the Rainbow vent site (36º14´N, MAR). *Chemical Geology, 216*(3-4), 329-352. https://doi.org/10.1016/j.chemgeo.2004.11.015

Coplen, T.B.; Kendall, C.; Hopple, J. (1983). Comparison of stable isotope reference samples. *Nature, 302*(5905), 236-238. https://doi.org/10.1038/302236a0

Dekov, V.M.; Cuadros, J.; Kamenov, G.D.; Weiss, D.; Arnold, T.; Basak, C.; Rochette, P. (2010). Metalliferous sediments from the HMS *Challenger* voyage (1872–1876). *Geochimica et Cosmochimica Acta*, *74*(17), 5019-5038. https://doi.org/10.1016/j.gca.2010.06.001

Dias, Á.; Barriga, F. (2006). Mineralogy and geochemistry of hydrothermal sediments from the serpentinite-hosted Saldanha hydrothermal field (36º34´N; 33º26´W) at MAR. *Marine Geology, 225*(1-4), 157-175. https://doi.org/10.1016/j.margeo.2005.07.013

Dias, Á.; Früh-Green, G.; Bernasconi, S.; Barriga, F. (2011). Geochemistry and stable isotope constrains on high-temperature activity from sediment cores of the Saldanha hydrothermal field. *Marine Geology, 279*(1-4), 128-140. https://doi.org/10.1016/j.margeo.2010.10.017

Douville, E.; Bienvenu, P.; Charlou, J.; Donval, J.; Fouquet, Y.; Appriou, P.; Gamo, T. (1999). Yttrium and rare earth elements in fluids from various deep-sea hydrothermal systems. *Geochimica et Cosmochimica Acta, 63*(5), 627-643. https://doi.org/10.1016/S0016-7037(99)00024-1

Douville, E.; Charlou, J.L.; Oelkers, E.H.; Bienvenu, P.; Colon, C.F.J.; Donval, J.P.; Prieur, D.; Appriou, P. (2002). The rainbow vent fluids (36°14′N, MAR): the influence of ultramafic rocks and phase separation on trace metal content in Mid-Atlantic Ridge hydrothermal fluids. *Chemical Geology*, *184*(1-2), 37-48. https://doi.org/10.1016/S0009-2541(01)00351-5

Dubinin, A. (2004). Geochemistry of rare earth elements in the ocean. *Lithology and Mineral Resources, 39*(4), 289-307. https://doi.org/10.1023/B:LIMI.0000033816.14825.a2

Dueñas, H.; Duque-Caro, H. (1981). Geología del Cuadrángulo F - 8 Planeta Rica. *Boletín Geológico, 24*(1), 1-35. https://doi.org/10.32685/0120-1425/bolgeol24.1.1981.264

Edmonds, H.N.; German, C.R. (2004). Particle geochemistry in the Rainbow hydrothermal plume, Mid-Atlantic Ridge. *Geochimica et Cosmochimica Acta, 68*(4), 759-772. https://doi.org/10.1016/S0016-7037(03)00498-8

Eickmann, B.; Little, C.T.S; Peckmann, J.; Taylor, P.D.; Boyce, A.J.; Morgan, D.J.; Bach, W. (2021). Shallow-marine serpentinization-derived fluid seepage in the Upper Cretaceous Qahlah Formation, United Arab Emirates. *Geological Magazine, 158*(9), 1561-1571. https://doi.org/10.1017/S0016756821000121

Elderfield, H. (1988). The oceanic chemistry of the rare-earth elements. *Philosophical Transactios of the Royal Society of London. Series A, Mathematical and Physical Sciences*, *325*(1583), 105-126. https://doi.org/10.1098/rsta.1988.0046

Escartín, J.; Mével, C.; MacLeod, C.J.; McCaig, A.M. (2003). Constraints on deformation conditions and the origin of oceanic detachments: The Mid-Atlantic Ridge core complex at 15°45´N. *Geochemistry, Geophysics, Geosystems, 4*(8). https://doi.org/10.1029/2002GC000472

Früh-Green, G.L.; Plas, A.; Lécuyer, C. (1996). Petrologic and stable isotope constraints on hydrothermal alteration and serpentinization of the EPR shallow mantle at Hess Deep (Site 895). *Proceedings of the Ocean Drilling Program Scientific Results, 147*, 109-163. https://doi.org/10.2973/odp.proc.sr.147.016.1996

Früh-Green, G.L.; Connoly, J.A.; Plas, A.; Kelley, D.; Grobéty, B. (2004). Serpentinization of oceanic peridotites: Implication for geochemical cycles and biological activity. In: W.S.D. Wilocock, E.F. Delong, D.S. Kelley, J.A. Baross, S.C. Cary (eds.). *The Subseafloor Biosphere at Mid-Ocean Ridges* (pp. 119-136). Vol. 144. Wiley. https://doi.org/10.1029/144GM08

Fu, Q.; Socki, R.A.; Niles, P.B. (2015). Evaluating reaction pathways of hydrothermal abiotic organic synthesis at elevated temperatures and pressures using carbon isotopes. *Geochimica et Cosmochimica Acta, 154*, 1-17. https://doi.org/10.1016/j.gca.2015.01.027

Gaudin, A.; Decarreau, A.; Noack, Y.; Grauby, O. (2005). Clay mineralogy of the nickel laterite ore developed from serpentinised peridotites at Murrin Murrin, Western Australia. *Australian Journal of Earth Sciences, 52*(2), 231-241. https://doi.org/10.1080/08120090500139406

German, C.R.; Higgs, N.C.; Thomson, J.; Mills, R.; Elderfield, H.; Blusztajn, J.; Fleer, A.P.; Bacon, M.P. (1993). A geochemical study of metalliferous sediment from the TAG hydrothermal Mound, 26°08´N, Mid-Atlantic Ridge. *Journal of Geophysical Research: Solid Earth, 98*(B6), 9683-9692. https://doi.org/10.1029/92JB01705

German, C.R.; Rudnicki, M.D.; Klinkhammer, G.P. (1999). A segment-scale survey of the Broken Spur hydrothermal plume. *Deep Sea Research Part I: Oceanographic Research Papers*, *46*(4), 701-714. https://doi.org/10.1016/S0967-0637(98)00078-8

German, C.R.; Von Damm, K.L. (2003). Hydrothermal processes. In: H. Elderfield (ed.). *The oceans and marine geochemistry: Treatise on Geochemistry* (pp. 181-222). Volume 6, Elsevier Ltd.

Gleeson, S.; Herrington, R.; Durango, J.; Velázquez, C.A.; Koll, G. (2004). The Mineralogy and Geochemistry of the Cerro Matoso S.A. Ni Laterite Deposit, Montelíbano, Colombia. *Economic Geology, 99*(6), 1197-1213. https://doi.org/10.2113/gsecongeo.99.6.1197

Grenne, T.; Slack, J.F. (2003). Paleozoic and Mesozoic silica-rich seawater: evidence from hematitic chert (jasper) deposits. *Geology, 31*(4), 319-322. https://doi.org/10.1130/0091-7613(2003)031<0319:PAMSRS>2.0.CO;2

Grenne, T.; Slack, J.F. (2005). Geochemistry of jasper beds from the Ordovician Løkken ophiolite, Norway: origin of proximal and distal siliceous exhalites. *Economic Geology, 100*(8), 1511-1527. https://doi.org/10.2113/gsecongeo.100.8.1511

Heath, G.R.; Dymond, J. (1981). Metalliferous-sediment deposition in time and space: East Pacific Rise and Bauer Basin, northern Nazca plate. In: L.V.D. Kulm.; J. Dymond; E.J. Dasch; D.M. Hussong; R. Roderick. (eds). *Nazca Plate: Crustal Formation and Andean Convergence* (pp.175-198). The Geological Society of America. https://doi.org/10.1130/MEM154-p175

Hein, J.R.; Koschinsky, A.; Halbach, P.; Manheim, F.T.; Bau, M.; Kang, J.K.; Lubick, N. (1997). Iron and manganese oxide mineralization in the Pacific. *Geological Society, London, Special Publications, 119*, 123-138. https://doi.org/10.1144/GSL.SP.1997.119.01.09

Hein, J.R.; Conrad, T.A.; Frank, M.; Christl, M.; Sager, W.W. (2012). Copper-nickel-rich, amalgamated ferromanganese crust-nodule deposits from Shatsky Rise, NW Pacific. *Geochemistry, Geophysics, Geosystems, 13*(10). https://doi.org/10.1029/2012GC004286

Hinkley, T.K.; Tatsumoto, M. (1987). Metals and isotopes in Juan de Fuca Ridge hydrothermal fluids and their associated solid materials. *Journal of Geophysic Research: Solid Earth, 92*(B11), 11400-11410. https://doi.org/10.1029/JB092iB11p11400

Hoefs, J.; Sywall, M. (1997). Lithium isotope composition of quaternary and Tertiary biogene carbonates and a global lithium isotope balance. *Geochimica et Cosmochimica Acta, 61*(13), 2679-2690. https://doi.org/10.1016/S0016-7037(97)00101-4

Hodel, F.; Macouin, M.; Trindade, R.I.F.; Triantafyllou, A.; Ganne, J.; Chavagnac, V., Berger, J.; Rospabé, M.; Destrigneville, C.; Carlut, J.; Ennih, N.; Agrinier, P. (2018). Fossil black smoker yields oxygen isotopic composition of Neoproterozoic seawater. *Nature Communications*, *9*(1), 1453. https://doi.org/10.1038/s41467-018-03890-w

Hongo, Y.; Obata, H.; Gamo, T.; Nakaseama, M.; Ishibashi, J.; Konno, U.; Saegusa, S.; Ohkubo, S.; Tsunogai, U. (2007). Rare Earth Elements in the hydrothermal system at Okinawa Trough back-arc basin. *Geochemical Journal, 41*(1), 1-15. https://doi.org/10.2343/geochemj.41.1

Hoyos, N.; Velázquez, C.A. (1996). Análisis del Origen de la Lateritización y Saprolitización del Yacimiento Niquelífero de Cerro Matoso. Tesis de Maestría, Universidad EAFIT, Medellín, Colombia.

Irwin, H.; Curtis, C.; Coleman, M. (1977). Isotopic evidence for source of diagenetic carbonates formed durign burial of organic-rich sediments. *Nature, 269*(5625), 209-213. https://doi.org/10.1038/269209a0

James, R.; Elderfield, H.; Palmer, M. (1995). The chemistry of hydrothermal fluids from the Broken Spur Site, 29ºN Mid-Atlantic Ridge. *Geochimica et Cosmochimica Acta, 59*(4), 651-659. https://doi.org/10.1016/0016-7037(95)00003-I

Johnson, C.; Beard, B.; Beukes, N.; Klein, C.; O`Leary, J. (2003). Ancient geochemical cycling in the Earth as inferred from Fe isotope studies of banded iron formations from the Transvaal Craton. *Contribution to Mineralogy and Petrology, 144*(5), 523-547. https://doi.org/10.1007/s00410-002-0418-x

Kelley, D.S.; Karson, J.A; Blackman, D.K.; Früh-Green, G.L.; Butterfield, D.A.; Lilley, M.D.; Olson, E.J.; Schrenk, M.O.; Roe, K.K.; Lebon, G.T.; Rivizzigno, P. (2001). An off-axis hydrothermal vent field near the Mid-Atlantic

Ridge at 30ºN. *Nature, 412*(6843), 145-149. https://doi.org/10.1038/35084000

Kelley, D.S.; Karson, J.A.; Früh-Green, G.L.; Yoerger, D.R.; Shank, T.M.; Butterfield, D.A.; Hayes, J.M.; Schrenk, M.O.; Olson, E.J.; Proskurowski, G.; Jakuba, M.; Bradley, A.; Larson, B.; Ludwig, K.; Glickson, D.; Buckman, K.; Bradley, A.S.; Brazelton, W.J.; Roe, K.; Elend, M.J.; Delacour, A.; Bernasconi, S.M.; Lilley, M.D.; Baross, J.A.; Summons, R.E.; Sylva, S.P. (2005). A serpentinite-hosted ecosystem: The Lost City Hydrothermal Field. *Science*, *307*(5714), 1428-1434. https://doi.org/10.1126/science.1102556

Klein, F.; Humphris, S.E.; Guo, W.; Schubotz, F.; Schwarzenbach, E.M.; Orsi, W.D. (2015). Fluid mixing and the deep biosphere of a fossil Lost City-type hydrothermal system at the Iberia Margin. *Proceedings of the National Academy of Sciences of the United States of America, 112*(39), 12036-12041. https://doi.org/10.1073/pnas.1504674112

Klinkhammer, G.; Elderfield, H.; Hudson, A. (1983). Rare earth elements in seawater near hydrothermal vents. *Nature*, *305*(5931), 185-188. https://doi.org/10.1038/305185a0

Klinkhammer, G.; Elderfield, H.; Edmond, J.; Mitra, A. (1994). Geochemical implications of rare earth element patterns in hydrothermal fluids from mid-ocean ridges. *Geochimica et Cosmochimica Acta, 58*(23), 5105-5113. https://doi.org/10.1016/0016-7037(94)90297-6

Kuhn, T.; Bau, M.; Blum, N.; Halbach, P. (1998). Origin of negative Ce anomalies in mixed hydrothermal–hydrogenetic Fe–Mn crusts from the Central Indian Ridge. *Earth and Planetary Science Letters, 163*(1-4), 207-220. https://doi.org/10.1016/S0012-821X(98)00188-5

Lartaud, F.; de Rafelis, M.; Oliver, G.; Krylova, E.; Dyment, J.; Ildefonse, B.; Thibaud, R.; Gente, P.; Hoisé, E.; Meistertzheim, AL.; Fouquet, Y.; Gaill, F.; Le Bris, N. (2010). Fossil clams from a serpentinite-hosted sedimented vent field near the active smoker complex Rainbow, MAR, 36º13'N: Insight into the biogeography of vent fauna. *Geochemistry, Geophysics, Geosystems*, *11*(8). https://doi.org/10.1029/2010GC003079

Lartaud, F.; Little, C.T.S.; de Rafelis, M.; Bayon, G.; Dyment, J.; Ildefonse, B.; Gressier, V.; Fouquet, Y.; Gaill, F.; Le Bris, N. (2011). Fossil evidence for serpentinization fluids fueling chemosynthetic assemblages. *Proceedings of the National Academy of Sciences of the United States of America*, *108*(19), 7698-7703. https://doi.org/10.1073/pnas.1009383108

Lavoie, D.; Chi, G. (2010). An Ordovician "Lost City"—venting serpentinite and life oases on Iapetus seafloor. *Canadian Journal of Earth Sciences, 47*(3), 199-207. https://doi.org/10.1139/E10-013

Lewis, J.F.; Draper, G.; Proenza, J.A.; Espaillat, J.; Jiménez, J. (2006). Ophiolite-related ultramafic rocks (Serpentinites) in the Caribbean region: A Review of their occurrence, composition, origin, emplacement and Ni-laterite soil formation. *Geologica Acta, 4*(1-2), 237-263. https://doi.org/10.1344/105.000000368

Li, X.; Jenkyns, H.C.; Wang, C.; Hu, X.; Chen, X.; Wei, Y.; Huang, Y.; Cui, J. (2006). Upper Cretaceous carbon- and oxygen-isotope stratigraphy of hemipelagic carbonate facies from southern Tibet, China. *Journal of the Geological Society, 163*, 375-382. https://doi.org/10.1144/0016-764905-046

Lilley, M.D.; Butterfield, D.A.; Olson, E.J.; Lupton, J.E.; Macko, S.A.; McDuff, R.E. (1993). Anomalous CH_4 and NH_4^+ concentrations at an unsedimented mid-ocean-ridge hydrothermal system. *Nature, 364*(6432), 45-47. https://doi.org/10.1038/364045a0

López-Rendón, J. (1986). Geology, mineralogy and geochemistry of the Cerro Matoso nickeliferous laterite, Córdoba, Colombia. MSc. Thesis, Colorado State University, Colorado, USA.

Ludwig, K.L.; Kelley, D.S.; Butterfield, D.A.; Nelson, B.K.; Früh-Green, G. (2006). Formation and evolution of carbonate chimneys at the Lost City Hydrothermal Field. *Geochimica et Cosmochimica Acta, 70*(14), 3625-3645. https://doi.org/10.1016/j.gca.2006.04.016

Marchig, V.; Gundlach, H.; Möller, P.; Schley, F. (1982). Some geochemical indicators for discriminating between diagenetic and hydrothermal metalliferous sediments. *Marine Geology,*

50(3), 241-256. https://doi.org/10.1016/0025-3227(82)90141-4

McLennan, S.M. (1989). Rare earth elements in sedimentary rocks: influence of provenance and sedimentary processes. In: B.R. Lipin, G.A. McKay (eds.). *Geochemistry and Mineralogy of Rare Earth Elements* (pp. 169-200). Vol. 21. https://doi.org/10.1515/9781501509032-010

McMurtry, G.M.; Burnett, W.C. (1975). Hydrothermal metallogenesis in the Bauer Deep of the south-eastern Pacific. *Nature, 254*(5495), 42-44. https://doi.org/10.1038/254042a0

McMurtry, G.M.; Yeh, H.W. (1981). Hydrothermal clay mineral formation of East Pacific rise and Bauer Basin sediments. *Chemical Geology, 32*(1-4), 189-205. https://doi.org/10.1016/0009-2541(81)90143-1

Mejia, V.M.; Durango, J.R. (1981). Geología de las lateritas niquelíferas de Cerro Matoso S.A. *Boletín de Geología, 15*(29), 99-116.

Meissnar, R.O.; Flueh, E.R.; Stibane, F.; Berg, E. (1976). Dynamics of the active plate boundary in southwest Colombia according to recent geophysical measurements. *Tectonophysics, 35*(1-3), 115-136. https://doi.org/10.1016/0040-1951(76)90032-9

Meister, P.; Wiedling, J.; Lott, C.; Bach, W.; Kuhfuß, H.; Wegener, G.; Böttcher, M.E.; Deusner, C.; Lichtschlag, A.; Bernasconi, S.M.; Weber, M. (2018). Anaerobic methane oxidation inducing carbonate precipitation at abiogenic methane seeps in the Tuscan archipelago (Italy). *PLoS One, 13*(12). https://doi.org/10.1371/journal.pone.0207305

Metz, S.; Trefry, J.H.; Nelsen, T.A. (1988). History and geochemistry of a metalliferous sediment core from the Mid-Atlantic Ridge at 26ºN. *Geochimica et Cosmochimica Acta, 52*(10), 2369-2378. https://doi.org/10.1016/0016-7037(88)90294-3

Mével, C. (2003). Serpentinization of abyssal peridotites at mid-ocean ridges. *Comptes Rendus Geoscience, 335*(10-11), 825-852. https://doi.org/10.1016/j.crte.2003.08.006

Michard, A.; Albarede, F.; Michard, G.; Minster, J.F.; Charlou, J.L. (1983). Rare-earth elements and uranium in high-temperature solutions from East Pacific Rise hydrolhermal vent field (13 ºN). *Nature*, *303*(5920), 795-797. https://doi.org/10.1038/303795a0

Michard, A.; Albarede, F. (1986). The REE content of some hydrothermal fluids. *Chemical Geology*, *55*(1-2), 51-60. https://doi.org/10.1016/0009-2541(86)90127-0

Mills, R.A.; Elderfield, H.; Thomson, J. (1993). A dual origin for the hydrothermal component in a metalliferous sediment core from the Mid-Atlantic Ridge. *Journal of Geophysical Research: Solid Earth, 98*(B6), 9671-9681. https://doi.org/10.1029/92JB01414

Mills, R.; Elderfield, H. (1995a). Hydrothermal Activity and the Geochemistry of Metalliferous Sediment. In: S.E. Humphris, R.A. Zierenberg, L.S. Mullineaux, R.E. Thomson (eds.). *Seafloor Hydrothermal Systems: Physical, Chemical, Biological, and Geological Interactions* (pp. 392-407). Vol. 91. American Geophysical Union. https://doi.org/10.1029/GM091p0392

Mills, R.; Elderfield, H. (1995b). Rare earth element geochemistry of hydrothermal deposits from the active TAG Mound, 26ºN Mid-Atlantic Ridge. *Geochimica et Cosmochimica Acta, 59*(17), 3511-3524. https://doi.org/10.1016/0016-7037(95)00224-N

Mitra, A.; Elderfield, H.; Greaves, M.J. (1994). Rare earth elements in submarine hydrothermal fluids and plumes from the Mid-Atlantic Ridge. *Marine Chemistry, 46*(3), 217-235. https://doi.org/10.1016/0304-4203(94)90079-5

Nozaki, Y. (2001). Rare earth elements and their isotopes in the Ocean. In: J.H. Steele (eds.). *Encyclopedia of Ocean Sciences* (pp. 2354-2366). Vol. 4. Academic Press Inc. https://doi.org/10.1006/rwos.2001.0284

Nozaki, Y.; Alibo, D.S. (2003). Importance of vertical geochemical processes in controlling the oceanic profiles of dissolved rare earth elements in the northeastern Indian Ocean. *Earth and Planetary*

Science Letters, 205(3-4), 155-172. https://doi.org/10.1016/S0012-821X(02)01027-0

Ortiz, F. (2004). Guías para la localización de metales preciosos en ofiolitas colombianas. Informe de avance proyecto Cyted XIII.1. Ofiolitas: Características mineralógicas y petrográficas del yacimiento de níquel de Cerro Matoso. *Dyna*, *71*(142), 11-23.

Palandri, J.L.; Reed, M.H. (2004). Geochemical models of metasomatism in ultramafic systems: serpentinization, rodingitization, and sea floor carbonate chimney precipitation. *Geochimica et Cosmochimica Acta*, *68*(5), 1115-1133. https://doi.org/10.1016/j.gca.2003.08.006

Peter, J.M.; Goodfellow, W.D. (1996). Mineralogy, bulk and rare earth element geochemistry of massive sulphide-associated hydrothermal sediments of the Brunswick Horizon, Bathurst mining camp, New Brunswick. *Canadian Journal of Earth Science, 33*(2), 252-283. https://doi.org/10.1139/e96-021

Pindell, J.; Barrett, S. (1991). Geological evolution of the Caribbean region: a plate tectonic perspective. In: G. Dengo, J.E. Case (eds). *The Caribbean Region* (pp. 405-432). Geological Society of America. https://doi.org/10.1130/DNAG-GNA-H.405

Pindell, J.L.; Kennan, L. (2009). Tectonic evolution of the Gulf of Mexico, Caribbean and northern South America in the mantle reference frame: an update. *Geological Society, London, Special Publications, 328*, 1-55. https://doi.org/10.1144/SP328.1

Piper, D.Z. (1974). Rare earth elements in the sedimentary cycle: a summary. *Chemical Geology, 14*(4), 285-304. https://doi.org/10.1016/0009-2541(74)90066-7

Piper, D.Z.; Graef, P.A. (1974). Gold and rare-earth elements in sediments from the East Pacific Rise. *Marine Geology*, *17*(5), 287-297. https://doi.org/10.1016/0025-3227(74)90092-9

Proskurowski, G.; Lilley, M.; Seewald, J.S.; Früh-Green, G.L.; Olson, E.J.; Lupton, J.E.; Sylva, S.P.; Kelley, D.S. (2008a). Abiogenic hydrocarbon production at Lost City hydrothermal field. *Science*, *319*(5863), 604-607. https://doi.org/10.1126/science.1151194

Proskurowski, G.; Lilley, M.D.; Olson, E.J. (2008b). Stable isotopic evidence in support of active microbial methane cycling in low-temperature diffuse flows vents at 9°50′N East Pacific Rise. *Geochimica et Cosmochimica Acta, 72*(8), 2005-2023. https://doi.org/10.1016/j.gca.2008.01.025

Rosenbaum, J.; Sheppard, S. (1986). An isotopic study of siderites, dolomites and ankerites at high temperatures. *Geochimica et Cosmochimica Acta, 50*(6), 1147-1150. https://doi.org/10.1016/0016-7037(86)90396-0

Ruhlin, D.E.; Owen, R.M. (1986). The rare earth element geochemistry of hydrothermal sediments from the East Pacific Rise: examination of a seawater scavenging mechanism. *Geochimica et Cosmochimica Acta, 50*(3), 393-400. https://doi.org/10.1016/0016-7037(86)90192-4

Savin, S.M.; Epstein, S. (1970). The oxygen and hydrogen isotope geochemistry of clay minerals. *Geochimica et Cosmochimica Acta, 34*(1), 25-42. https://doi.org/10.1016/0016-7037(70)90149-3

Sciarra, A.; Saroni, A.; Etiope, G.; Coltorti, M.; Mazzarini, F.; Lott, C.; Grassa, F.; Italiano, F. (2019). Shallow submarine seep of abiotic methane from serpentinized peridotite off the Island of Elba, Italy. *Applied Geochemistry, 100*, 1-7. https://doi.org/10.1016/j.apgeochem.2018.10.025

Shank, T.M.; Fornari, D.J.; von Damm, K.L.; Lilley, M.D.; Haymon, R.M.; Lutz, R.A. (1998). Temporal and spatial patterns of biological community development at nascent deep-sea hydrothermal vents (9°50′N, East Pacific Rise). *Deep Sea Research Part II: Topical Studies in Oceanography*, *45*(1-3), 465-515. https://doi.org/10.1016/S0967-0645(97)00089-1

Sherrell, R.M.; Field, M.; Ravizza, G. (1999). Uptake and fractionation of rare earth elements on hydrothermal plume particles at 9°45′N, East Pacific Rise. *Geochimica et Cosmochimica Acta, 63*(11-12), 1709-1722. https://doi.org/10.1016/S0016-7037(99)00182-9

Slack, J.F.; Grenne, T.; Bekker, A.; Rouxel, O.J.; Lindberg, P.A. (2007). Suboxic deep seawater in

the late Paleoproterozoic: Evidence from hematitic chert and iron formation related to seafloor-hydrothermal sulfide deposits, central Arizona, USA. *Earth and Planetary Science Letters,* 255(1-2), 243-256. https://doi.org/10.1016/j.epsl.2006.12.018

Slack, J.F.; Grenne, T.; Bekker, A. (2009). Seafloor-hydrothermal Si-Fe-Mn exhalites in the Pecos greenstone belt, New Mexico, and the redox state of ca. 1720 Ma deep seawater. *Geosphere*, *5*(3), 302-314. https://doi.org/10.1130/GES00220.1

Sumicol (2002). Caracterización mineralógica de los tipos de roca de la laterita niquelífera de Cerro Matoso S.A. Colombia. Informe de investigación para Cerro Matoso S.A.

Templeton, A.S.; Staudigel, H.; Tebo, B.M. (2005). Diverse Mn(II)-oxidizing bacteria isolated from submarine basalts at Loihi Seamount. *Geomicrobiology Journal, 22*(3-4), 127-139. https://doi.org/10.1080/01490450590945951

Tobón, M.; Weber, M.; Proenza, J.A.; Aiglsperger, T.; Betancur, S.; Farré-de-Pablo, J.; Ramírez, C.; Pujol-Solà, N. (2020). Geochemistry of Platinum-Group Elements (PGE) in Cerro Matoso and Planeta Rica Ni-Laterite deposits, Northern Colombia. *Boletín de la Sociedad Geológica Mexicana, 72*(3), A201219. https://doi.org/10.18268/BSGM2020v72n3a201219

Tostevin, R.; Shields, G.A.; Tarbuck, G.M.; He, T.; Clarkson, M.; Wood, R.A. (2016). Effective use of cerium anomalies as a redox proxy in carbonate-dominated marine settings. *Chemical Geology, 438*, 146-162. https://doi.org/10.1016/j.chemgeo.2016.06.027

Sui, A.U.; Lasby, G.P.G. (1998). Submarine hydrothermal manganese deposits in the Izu–Bonin–Mariana Arc: an overview. *Island Arc, 7*(3), 422-431. https://doi.org/10.1111/j.1440-1738.1998.00200.x

Whiticar, M.J.; Faber, E. (1986). Methane oxidation in sediment and water column environments—isotopic evidence. *Organic Geochemistry, 10*(4-6), 759-768. https://doi.org/10.1016/S0146-6380(86)80013-4

Zhang, C.L.; Horita, J.; Cole, D.R.; Zhou, J.; Lovley, D.R.; Phelps, T.J. (2001). Temperature-dependent oxygen and carbon isotope fractionations of biogenic siderite. *Geochimica et Cosmochimica Acta, 65*(14), 2257-2271. https://doi.org/10.1016/S0016-7037(01)00596-8

Received: 02 March 2022
Accepted: 02 November 2022